DESIGN OF INFRARED MICROSCOPE

by

Kai Hu

A Thesis Submitted to the Faculty of the

COLLEGE OF OPTICAL SCIENCES

In Partial Fulfillment of the Requirements

For the Degree of

MASTER OF SCIENCE

In the Graduate College

THE UNIVERSITY OF ARIZONA

2019

THE UNIVERSITY OF ARIZONA
GRADUATE COLLEGE

As members of the Master's Committee, we certify that we have read the thesis prepared by Kai Hu, titled Design of Infrared Microscope and recommend that it be accepted as fulfilling the dissertation requirement for the Master's Degree.

Tom Milster — Date: 4/30/2019

Euan McLeod — Date: 4/30/19

Khanh Kieu — Date: 04/30/19

Final approval and acceptance of this thesis is contingent upon the candidate's submission of the final copies of the thesis to the Graduate College.

I hereby certify that I have read this thesis prepared under my direction and recommend that it be accepted as fulfilling the Master's requirement.

Tom Milster — Date: 5/9/2019

Tom Milster
Master's Thesis Committee Chair
College of Optical Sciences

ACKNOWLEGEMENTS

The thesis accomplishment takes a lot effort and I am really thankful to my advisor Tom Milster for he can always guide me to the right track and give me some inspiration that really helpful to my research. Also, I would like to thank College of Optical Sciences. In the department I learned a lot of diverse content so that I can combine all the techniques I learn to tackle the ways out in my research. Also, very thankful to some of the staff in University of Arizona library that when my computer broke down and lost my thesis. They are very kind to help me and offer a computer to use to back up my files.

TABLE OF CONTENTS

LIST OF FIGURES

LIST OF TABLES

A B S T R A C T

This thesis introduces a way to arrange the setup of infrared microscope so that it is theoretically feasible to realize the experimental infrared microscope. The most challenging problem mainly resolved in this paper is how to increase the really low SNR from 10^{-8} to a measurable value. The process includes introducing an Optical Amplifier, such as Quantum Cascade Laser Amplifier, and applying sensitive detector, such as HgCdTe PD/APD with lock-in Amplifier. Finally, we also discuss about a way to arrange the infrared optical system and introduce a sample design of a high NA infrared objective (NA=3.7).

Introduction

An intriguing challenge is to directly image sub-cellular metabolism noninvasively by thermal imaging. Applications include increasing cancer cell detection rates [13] , studying the mechanism of cancer cell metabolism [14] and other cell metabolism [15] The difficulty to realize this goal is due to basic infrared optical engineering tradeoffs. Cells typically live in the temperature range of (271+31)K to (271+35)K, so imaging temperature distributions means imaging microscopic light sources that emit with a peak wavelength of around 10μm. Unlike microscopes, most infrared systems have a large detection object area, so the signal is detectable with good signal-to-noise ratio. However, a primary reason we still lack general-purpose infrared microscopes today is because of the very weak signal caused by differences in temperature between small detection areas associated with sub-cellular organelles. In addition, since the microscope works in the infrared spectrum, the spatial resolution, which is proportional to the wavelength λ, is very poor compared to visible-light microscopes. Unfortunately, many optical super-resolution techniques like the confocal microscope, structured illumination, or STED cannot be used in an infrared microscope system because we cannot use illumination system in the microscope. Besides the spatial resolution and signal to noise ratio (SNR) issues, the small thermal resolution is another important aspect of the problem. The thermal resolution in most of today's thermometry techniques is about 0.1K, which is the fluctuation of the average temperature of a large bulk of cells. On a sub-cellular scale, the fluctuation might vary from 0.01K to 0.001K. If we really want to see these small differences in temperature due to metabolic activity within a cell, a new type of microscope is needed. The goal of this thesis is to understand the necessary engineering to achieve ultra-high thermal resolution as high as possible (0.001K) while maintaining high spatial resolution (1μm), without introducing any exogenous materials into the cell or damaging the cell with high laser power.

As we know that there are plenty of optical instruments, microscopes, spectroscopies nowadays in multiple applications that advance chemistry, biology, medicine and even optics. But still very limited types of infrared apparatus are undertaken for academic or industrial promotion. The reasons for that are the very limited and costly available materials, radiation sources, and detectors that lay a barrier for engineering development for infrared system. In

the spectrum of visible light, we can very easily set up a microscope to detect cell, but in infrared spectrum, many different situations need to be considered. The common applications for infrared spectrum are, for example thermal detection, or spectroscopy. The following techniques relate to our cellular thermal detection and are valuable for us to evaluate.

Fourier Transform Infrared Spectroscopy (FTIR) is commonly used in chemistry and biological research, and it also is very efficient in medical diagnoses. A near-field microscope combining FTIR to discriminate SiO_2, SiC, Si_xN_y, and TiO_2 in a thin film used in semiconductor technology [1] and a microscopic FTIR that identifies normal and cancerous colonic tissues by evaluating phosphate and creatine contents [2] show examples of chemical and medical FTIR applications in material discrimination. The principle of FTIR is to use a broad infrared spectrum source, for example synchrotron radiation, and a Michelson interferometer to split the responsive wavelength of the sample. Due to different vibrational structure of various materials causing different absorption spectrum, application of a Fourier Transform to a series of images, we can form a spectroscopic image that can identify different materials. Although it has been widely used, we cannot apply this technique to our cellular thermal detection, because it is materials detection oriented not for thermometry.

However, there is a biological technique [3] that uses materials to detect temperature variance within the cell. What they do is label the cell with dye Rhodamine B (RhB), which is a fluorescent dye whose fluorescence intensity decreases linearly with increases in temperature. And with a microfluorimetry setup, we can detect the temperature variance within the cell by detecting fluorescence intensity radiated by RhB. But unfortunately, this technique has the thermal resolution limited to 1K. The other similar technique called fluorescent polymeric thermometer (FPT) [56] use a poly-*N*-*n*-propylacrylamide (NNPAM) sequence, whose hydration process is affected by the temperature, then the number of water molecules will fluctuate so that DBD-AA unit can have different fluorescence lifetime so that we can measure to make a temperature mapping with confocal fluorescence microscope. The thermal resolution is reported to have $0.18 - 0.58℃$.

Temperature measurement can also be made using the thermal conduction, which is very common in thermometry. The scanning thermal microscope (SThM) [4] is invented based on this principle. The invention of the scanning tunneling microscope (STM) and atomic force microscope (AFM) led to this type of thermal microscope. SThM uses a thermocouple probe scanning across a nanostructured material surface to detect sub-surface temperature with tip-sample heat transfer mechanism. A small gap controlled by the AFM cantilever is very

important to make stable thermal conduction. So SThM can achieve spatial resolution of 500nm resolution. Also, the best resolution of thermocouples can obtain is typically 0.1mK.

Another important technique for temperature measurement is called laser reflectance thermometry. The basic foundation of this technique is based on the thermoreflectance effect on the surface of the materials. A laser beam illuminates the material surface, and the intensity from the reflected light is dependent on the temperature of the material so that we can indirectly measure the temperature. This technique has been demonstrated [5] by testing a surface of p-doped resistor in an IC with lateral resolution of $1\mu m$ and temperature resolution $10^{-3}\,°C$. However, reflectivity is not only dependent on temperature, it also depends on topography of the surface, if the light is scattered by the roughness or defect of the surface, the intensity is different in a specific direction. Another approach is to use the near field [6]. The approach is very similar to the near-field scanning optical microscope (NSOM)[55]. A tapered metallic fiber tip is used with a cantilever to control the tip-surface separation for stabilized thermal signal collection, similar to AFM. Two objectives are used to collect the reflective and transmitted radiation from the sample. So, three channels are combined to determine the temperature with higher accuracy. This technique can increase spatial resolution by two orders of magnitude.

Another technique for microscopic thermometry is called micro-Raman spectroscopy, which is explained in [7]. The principle of Raman spectroscopy is based on the frequency change of incident laser light that is scattered inelastically by elementary excitations within the crystal, which is called Raman scattering. Raman scattering includes both Stokes and Anti-Stokes processes that are symmetric to the incident light frequency. In a Stokes Raman process, the incident photon creates an optical phonon, and the rise of lattice temperature is observed through the energy shift of the optical lattice vibration – optical crystal phonon. With a spectrometer, we can observe a shift of the spectrum peak of the collected light scattered by the sample as it is deviated from the spectrum peak of the incident light due to the temperature modulation in the sample. This technique can not only measure surface temperature (opaque materials) but also internal temperature (transparent materials), so it is widely used. But the temperature resolution in [7] is also very limited to $\Delta T = \pm 2K$. There are also other Raman spectroscopies that are used for biological purpose, for example, confocal Raman micro-spectroscopy to study spontaneous death process of a single budding yeast [8] or the Coherent Anti-Stokes Raman Scattering (CARS) microscope to image the cell with high resolution [9]. One thing that should be noticed is that Raman scattering can be used both for materials identification and thermal measurement. But this spectroscopy technique is more suitable for

materials recognition for it is more sensitive to vibrational mode of materials than the thermal shift. So, it has limited thermal resolution.

FTIR can be combined with visible light to transform the IR spectrum into a visible spectrum in order to gain higher spatial resolution due to the smaller diffraction limit of visible light. Two similar techniques were proposed with this principle. One is called transient fluorescence detected IR (TFD-IR) spectroscopy [10], and the other is called vibrational sum-frequency generation (VSFG) IR super-resolution microscope [11]. TFD-IR uses a visible beam with its wavelength slightly longer than the absorption band of dyed fluorescent molecule Rhodamine-6G, so that we cannot detect a fluorescent signal at first. But, after the scanned-spectrum IR beam is introduced and if it is exactly set to vibrational mode of the molecules, the molecules are pumped to an excited state and emit fluorescent light. Thus, the IR information is transferred to visible fluorescent information. But this technique is limited to fluorescent samples. So, the VSFG microscope is introduced based on a non-linear effect called vibrational sum-frequency generation. The method uses visible photons and IR photons to illuminate the molecule, and a new photon with its energy equal to the sum frequency of the first two photons is emitted by the molecule. If the IR photon is resonant to the vibrational modes of sample molecule, the VSFG signal is detected, and by scanning the spectrum of IR wavelength we can obtain the IR spectrum of the sample by recording the visible light intensity. The VSFG effect is applicable to non-fluorescent dyes, but it is limited to materials with non-inversion symmetry, i.e. materials composed of chiral chemical species. Materials with inversion symmetry, like water, and glass do not have such an effect. Fortunately, most biological molecules have chirality that can emit VSFG light.

There is also another microscope that uses a non-linear effect using IR technology [12], which is called non-linear optical infrared (NLIR) microscopy. NLIR microscopy is based on the thermal Kerr effect that is induced by mid-wave IR (MWIR) energy. The refractive index changes proportionally with the square of the MWIR intensity and also with the linear spectral absorption coefficient of the sample, so that the chemical characteristics of the sample are dependent on the absorption coefficient. A visible ray radiates collinearly with the MWIR ray to the sample, so if the MWIR modulates the reflective index of the sample, the visible ray will deflect causing wavefront distortion. So, we can detect the deflection to determine the chemical characteristics of the sample. This principle is very similar to laser reflection technique: Reflectivity modulated by temperature as opposed to reflective index modulated by MWIR; signal collected by laser reflectance as opposed to signal collected by laser transmission. But even though this technique can achieve $0.7\mu m$ resolution with

633nm laser ray, this technique only can be applied to materials identification not the thermometry.

In summary, many techniques are available to compensate for the shortage of an IR microscope for materials identification or thermometry, as shown in Table 1 below. FTIR, VSFG, NLIR microscope and Raman spectroscopy are mainly used for materials identification, while RhB fluorescence microscope, SThM, laser reflectance, and some thermally intended micro-Raman spectroscopy mainly for thermometry. SThM can only detect surface temperature, and the tip probe's signal is largely affected by the gap between sample, RhB fluorescence is a good choice, but the thermal resolution is limited to 1K, and it is hard to improve higher due to RhB chemical characteristics. Laser reflectance is limited to the surface temperature regime, and the strong field laser may affect cell behavior, for example absorption by the cell materials. Micro-Raman spectroscopy has a problem of low thermal resolution. These techniques exhibit either too low temperature resolution, depend on exogenous dyes, are invasive, or must use high laser power. Therefore, there is a need for a true IR microscope with both fine thermal resolution and good spatial resolution.

Method	Detection Type	Thermal Resolution ΔT	Time Resolution δt	Advantage	Disadvantage
FTIR	Material Detection			Widely used in spectroscopy	Not for thermometry
Dye RhB Fluorescence /FPT	Thermometry	1K /0.1K	10μs	Use fluorescence visible light instead of infrared	The thermal resolution is low
SThM	Thermometry	0.1mK	10^2μs	High thermal and spatial resolution	Only for surface detection
Laser Reflectance	Thermometry	1mK	0.1μs	High thermal resolution	Can harm cell and only for surface detection
Raman Spectroscopy /Thermometry	Material Detection /Thermometry	2K	1s	Both surface and internal temperature	Thermal resolution is low

TFD-IR/VSFG IR microscope	Material Detection	Can transfer infrared to visible spectrum	Not generally applied to all materials
NLIR microscope	Material Detection	High spatial resolution	For material detection

Table 1 Thermal techniques that related to microscopy design [57]

In this thesis, we intend to evaluate the feasibility or possibility of setting up an IR microscope. And then we give a brief schematic of IR microscope and a sample of IR objective that may favor future development of such device. Chapter 1 will discuss our calculation model of the cell and evaluate the SNR in a traditional microscopic system. Chapter 2 will evaluate two schemes of optical amplifier in order to increase SNR. Chapter 3 introduces multiple low-noise infrared detectors that we probably use in the microscope. Chapter 4 is the infrared microscope system design and we give a sample of objective design for the infrared microscope.

Chapter 1. Theoretical Calculation

1.1 Object Model of Detected Cell

To realize this new kind of infrared microscope in optical way. First, we need to prove that this idea is feasible. So, the first step to design such microscope is to model the whole system in an ideal theoretical way and make the issue and situation easy to be evaluated and calculated. And then we can engineer each module of the microscope with the modern technology to make our goals come true.

First, we model a special case that can generalize most of the cases when we are doing the biological detection and observation towards the cell. Since there are thousands of cells with different properties and physiological characteristics, we cannot analyze case by case and cannot adjust the optical system to detect a specific sort of cell for it is too complex to design such a system. So, if we have an optical microscope that can cover most of the detection cases, that should be significant in medical treatment. And with the first prototype, the derivatives of this microscope will appear to extend a larger scale of cell detection. So, for the prototype of infrared microscope, we lead it to detect one of the most typical cells in human body — muscle cell. This type of cell is ideal because it is large compared to the other cells, typically with 40μm to 60μm diameter and with millimeters to centimeters length. Also, muscle cell is the most valuable cell to study cellular metabolism because it is the fuel engine for body movement. As the infrared wavelength is long, for example, if we use Long wavelength infrared (LWIR) light 8μm-15μm to detect the radiation of the cell. The resolution is limited by the diffraction limit about half of the wavelength with NA=1, which is about 4μm-7μm. So, with this resolution, we can somewhat localize the temperature gradient within the muscle cell. But, this resolution is not enough in other cell detection, because there’re many cells much smaller than muscle cells with 10μm-20μm diameter. So, to be more general, the resolution should be more strictly restricted to 1μm to be ideally applied in real case. To achieve this, we need some super-resolution or sub-wavelength techniques to make the microscope exceed the diffraction limit. But in theoretical calculation, first, we ignore this issue to make the problem easier to understand.

Therefore, we can set up a model as a detection environment for the infrared microscope:

1. Object Area of differential temperature/ Resolution: $A_{object} = 1\mu m \times 1\mu m$
2. Size of the cell (typical muscle cell): $A_{cell} = 40\mu m \times 40\mu m$
3. Temperature of background: $T_{background} = 38℃$
4. Average Temperature of cell: $T_{cell} = 38℃$
5. Differential Temperature of the object area: $\Delta T_{object} = 0.001K$

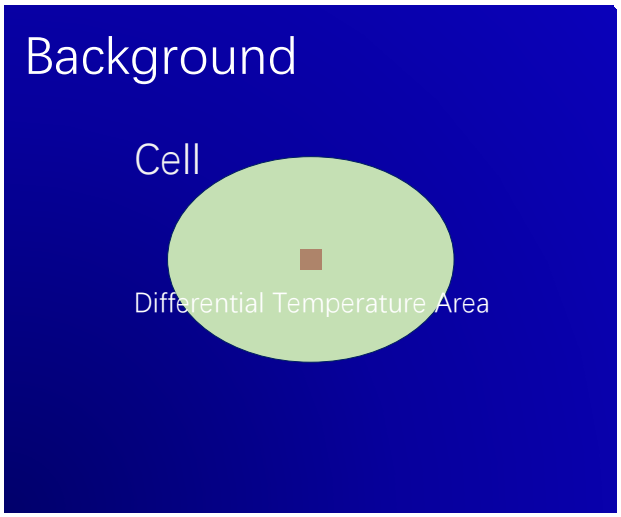

Figure 1. 1 Cell Object Model: the square area in the middle is regarded as different temperature area with the rest part of the cell. This area is also the smallest resolved area of the microscope.

1.2 Blackbody Radiation Model

The cell act as a source itself radiating thermal radiation. This thermal radiation is the information and signal that we need to collect and dispose. To make the problem easy to evaluate, we assume the cell as an ideal blackbody. But actually, the cell is never to be ideal blackbody because of the spatial dependent emissivity, so sometimes we need emissivity correction technology [16] to get the true temperature distribution information. But in this theoretical calculation, we consider the emissivity to be constant to make the problem become easier to evaluate. So, in this case, the emissivity is set to 1. Then we can have Plank's blackbody radiation curve [17] to calculate the cell's monochromatic radiated emittance(Watt/m^2 ·wavelength):

$$Md\lambda = \frac{2\pi hc^2}{\lambda^5\left(e^{\frac{hc}{\lambda k_B T}}-1\right)}d\lambda \qquad (1.\ 1)$$

Where h is Plank's constant, c is the velocity of light in vacuum, k_B is Boltzmann's constant, T is the temperature in Kelvins.

And with Wien's displacement law

$$\lambda_{\text{peak}} T = 2897.8\ \mu m \cdot K \tag{1. 2}$$

substitute $T_{cell} = 38℃ = 311K$ into the equation we get the peak wavelength is

$$\lambda_{peak} = 9.3177\mu m \tag{1. 3}$$

This is the wavelength radiating the highest emittance in the cell. It means most of the radiation spectrum of the cell is lying in LWIR spectrum. And if we change the temperature with 5℃, for example from 35℃ to 40℃. The peak wavelength changes a little.

$$\lambda_{peak} = 9.2581\mu m \sim 9.4084\mu m \tag{1. 4}$$

Therefore, we can ignore the wavelength shift in real case when measuring the temperature difference.

In order to evaluate the signal performance in the detector, we choose Thorlabs 10.6μm VML10T0 photodiode as an example.

VML10T0 Specification:

1. Effective Area: $A = 1mm^2$
2. Detectivity: $D^* \geq 1.0 \times 10^8 cm \cdot \sqrt{Hz}/W$
3. Operating Temperature: $T = 27℃$
4. Storage Temperature: $T = -23℃ \sim 47℃$
5. Wavelength range: $\lambda = 2.5\mu m \sim 10.6\mu m$

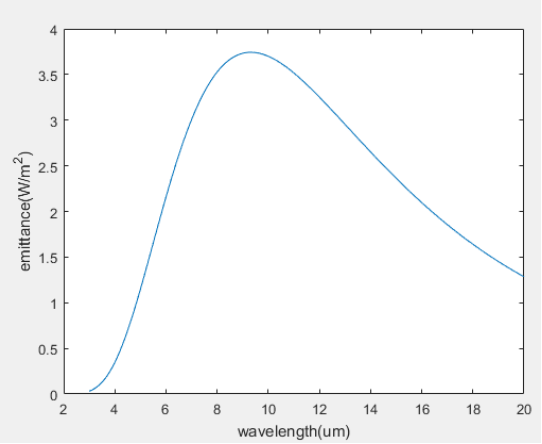

Figure 1. 2 Blackbody Emittance Versus Wavelength: we can see that the peak wavelength is around 9~10μm

So we can cut up the detector's wavelength range into

$$\lambda = 3\mu m \sim 10\mu m \tag{1. 5}$$

Then, the total emittance of the cell average radiation can be calculated with wavelength integral:

$$M_{cell}^{T=38°C} = \int_{3\mu m}^{10\mu m} M d\lambda = \int_{3\mu m}^{10\mu m} \frac{2\pi hc^2}{\lambda^5 (e^{\frac{hc}{\lambda k_B T}} - 1)} d\lambda \tag{1. 6}$$

The result is

$$M_{background}^{T=38°C} = 158.0156\ \mathrm{W}/m^2 \quad (1.7)$$

this radiation can be seen as the background emittance when we are localizing and detecting a specific area of the cell

And the total emittance of the object calculated with $T_{object} = T_{cell} + \Delta T_{object} = 38.001℃$ can be seen as the fluctuation of temperature in a small area of the cell, and this fluctuation of temperature is what we need as the information of cellular metabolism:

$$M_{object}^{T=38.001°C} = \int_{3\mu m}^{10\mu m} M d\lambda = \int_{3\mu m}^{10\mu m} \frac{2\pi hc^2}{\lambda^5 (e^{\frac{hc}{\lambda k_B T}} - 1)} d\lambda \quad (1.8)$$

The result is

$$M_{background}^{T=38.001°C} = 158.0188\ \mathrm{W}/m^2 \quad (1.9)$$

Then the signal is the difference of these two emittances:

$$\Delta M = M_{object}^{T=38°C+\Delta T} - M_{background}^{T=38°C} = 0.0032\mathrm{W}/m^2 \quad (1.10)$$

1.3 Relationship Between Blackbody's Emittance and Temperature

If we calculate the total emittance vs temperature relationship and draw a plot. We can find that the relationship between blackbody's Emittance and temperature is almost linear when the temperature varies within 5℃.

If we do the linearity fit with the M vs T curve, this fit is really good and what is means is that emittance is increasing linearly with temperature, the slope of the curve is

$$slope = 3.1951\ W/m^2 \cdot K \quad (1.11)$$

This relationship is almost true up to a temperature range of 20℃:

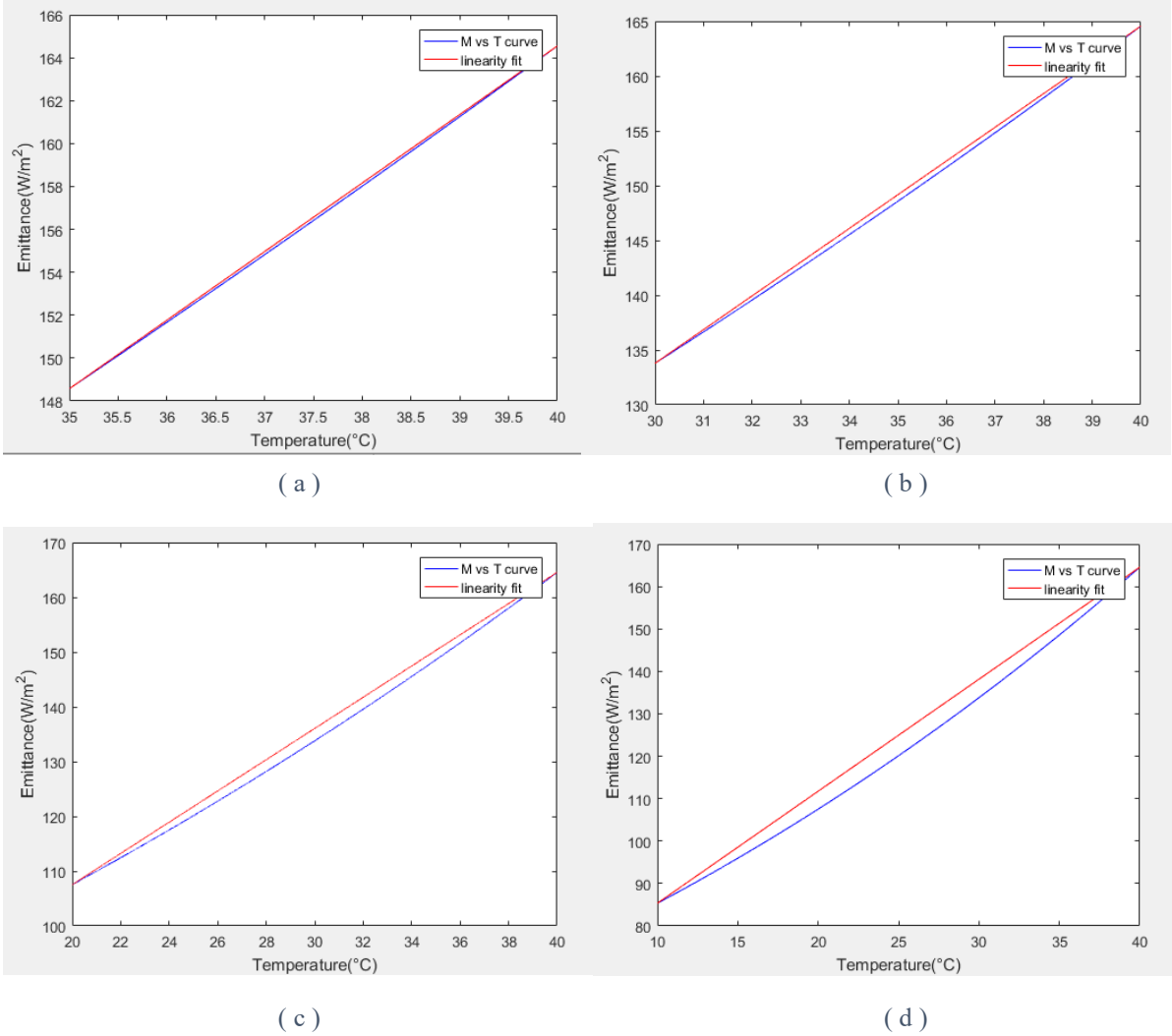

Figure 1. 3 Emittance versus Temperature: (a) Temperature range from 35℃~40℃ (b) Temperature range from 30℃-40℃ (c) Temperature range from 20℃-40℃ (d) Temperature range from 10℃-40℃. Note that the linearity fit is perfect within a temperature range of 20℃ around human temperature.

This relationship is the basis of linear temperature imaging, which means we can determine the temperature directly from the intensity of the infrared light radiated from the cell without using complicated nonlinear image processing method to get the temperature distribution of the cell. So the relationship of emittance and the differential temperature can be approximate with the following formula:

$$\Delta M = slope \times \Delta T \qquad (1.\ 12)$$

To verify this approximation, we simply substitute the slope value $slope = 3.1951\ W/m^2 \cdot K$ and $\Delta T = 0.001K$, we can get the result $\Delta M = 0.003195\ W/m^2$, which is almost the same as the result (1. 10) calculated with wavelength integral. In the following method, we

use this approximation to obtain the temperature value from the intensity signal captured by the detector.

1.4 Paraxial Microscope Optical System Simulation

In order to see the system performance in the most general optical system, we use very simple specification with unit magnification:

1. Focal length of the first lens: $f_1 = 50mm$
2. Focal length of the second lens: $f_2 = 50mm$
3. Thickness: $t = 100mm$
4. Diameter of two lenses: $D = 50mm$
5. F/# number: $f/1$
6. Magnification: $|m| = 1$

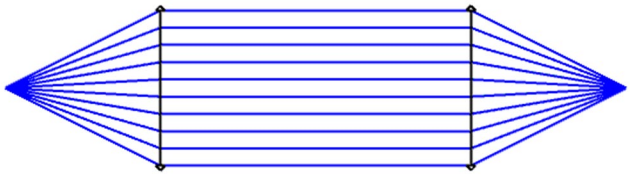

Figure 1. 4 Paraxial Microscope Imaging System Model: To simplify for our calculation we assume the microscope magnification to be 1, so the tube lens focal length and the objective lens focal length is eqaul

The reason why we choose the confocal method is because with the scanning method, we can image the cell with only the on-axis optical information, which drastically reduces the load of aberration correction work in designing objective lens without considering off-axis aberration such as coma, astigmatism. These advantages give us more space and freedom for us to adjust other more important aspect, for example increasing NA, for better performance. Scanning confocal method can let us achieve diffraction limit imaging more easily, which is really advantageous to attain our resolution goal. However, in thermal detection method, what makes this optical system different is that this scanning confocal infrared optical system do not include illumination system. This is because the cell or object itself actively act as the thermal radiation source, which is different from conventional optical system with the object

passively illuminated with a light source. So, for this reason, we do not include illumination system.

But also for this reason, we need to calculate how many light can we collect in order to make sure the signal can be captured and recognized. The throughput of the optical system can be calculated using the formula:

$$Throughput = A\Omega \tag{1. 13}$$

In which, the area of the object is

$$A = 1\mu m \times 1\mu m \tag{1. 14}$$

The solid angle Ω can be calculated using the following formula:

$$\Omega = \frac{\pi D^2}{4f_1^2} \tag{1. 15}$$

So the throughput of the system is

$$Throughput = \frac{A \times \pi D^2}{4f_1^2} = 7.854 \times 10^{-13}\ m^2 \cdot sr \tag{1. 16}$$

System radiation power can be calculated as followed

$$P = LA\Omega = Throughput \times \frac{M}{\pi} \tag{1. 17}$$

If we don't consider the transmissive lost of the power, the background radiation power through the optical system is

$$P_{background} = throughput \times \frac{M_{background}^{38°C}}{\pi} = 3.9504 \times 10^{-11}\ W \tag{1. 18}$$

The signal power is

$$\Delta P = throughput \times \frac{\Delta M}{\pi} = 8.0476 \times 10^{-16}\ W \tag{1. 19}$$

1.5 Noise analysis

1.5.1 Photon Shot Noise

Photon shot noise is coming from background radiation. So, to reduce this noise, we need to control the environmental detection temperature and keep it low to introduce noise as little as possible and at the same time not too low to kill the cell. So we need cooling system. And to prevent the noise coming from light traveling, the whole optical system should also be isolated from the external environment and needs to be cooled as well.

If the number of photons is large, photon shot noise can be approximated as Gaussian distribution instead of Poisson distribution. The variance of the shot noise is calculated as:

$$\sigma_{shot\ noise} = \sqrt{N} \tag{1. 20}$$

Where N is the average number of background photons. To obtain the number of photons in background radiation and signal radiation, we use the formula as below:

$$N = throughput \times \int_{3\mu m}^{10\mu m} \frac{M d\lambda}{\pi h v} \tag{1. 21}$$

Then the background photons' number is

$$N_{background} = 1.5265 \times 10^{9} s^{-1} \tag{1. 22}$$

Signal photons' number is

$$\Delta N = 2.9686 \times 10^{4} s^{-1} \tag{1. 23}$$

So we can calculate the Signal to Noise Ratio(SNR) using the definition of the photon shot noise:

$$SNR_{optics} = \frac{\Delta N}{\sqrt{N_{background}}} = 0.7598 \tag{1. 24}$$

With SNR, we can approximate the noise equivalent power of photon shot noise:

$$NEP_{optics} = \frac{\Delta P}{SNR_{optics}} = 1.0591 \times 10^{-15}\ W \tag{1. 25}$$

1.5.2 Electrical Noise Introduced By The Detector

Photon shot noise is a kind of noise that come from optical system. So it is a noise existed in light that we cannot avoid facing it when we use optical detection. But when the light is collected by the detector and undergone an opto-electrical transformation. The detector will also add another electrical noise into the electrical signal we get. And after calculation, we will find that this is the main noise source in this process of detection.

All of the electrical noises introduced by the detector can be expressed in total by using detectivity of the detector D^*. And with its detecting area A and working bandwidth Δf, we can use the formula below to calculate electrical noise equivalent power $NEP_{electrical}$:

$$NEP_{electricity} = \frac{\sqrt{A\Delta f}}{D^*} \tag{1. 26}$$

The data sheet of VML10T0 has a recommended circuit of VML10T0, in which contain a low pass noise filter. With this filter, we can calculate the detector's working bandwidth by using the formula below:

$$\Delta f = \frac{1}{2\pi RC} \tag{1. 27}$$

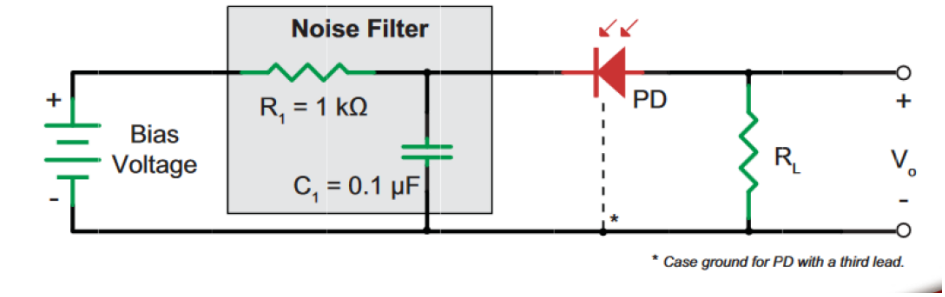

Figure 1. 5 VML10T0 Noise Filter Circuit

Substitute $R = 1k\Omega,\ C = 0.1\mu F$ into the formula, we can get the working bandwidth of the photodiode

$$\Delta f = 1591.5\text{Hz} \tag{1. 28}$$

Therefore, substitute this value into (1. 26) , and with $A = 1mm \times 1mm,\ D^* = 1 \times 10^8\ cm \cdot \sqrt{Hz}/W$, we can get the electrical noise equivalent power is

$$NEP_{electricity} = \frac{\sqrt{A\Delta f}}{D^*} = 3.9894 \times 10^{-8}\ W \tag{1. 29}$$

Therefore, electrical Signal to Noise Ratio can be calculated as followed:

$$SNR_{electricity} = \frac{\Delta P}{NEP_{electronics}} = 2.0173 \times 10^{-8} \tag{1. 30}$$

1.6 Conclusion

From the calculation above, we briefly list the calculation's result as below:

Signal:

$$\Delta P = 8.0474 \times 10^{-16}\ W \tag{1. 31}$$

$$\Delta N = 2.9686 \times 10^{4} s^{-1} \tag{1. 32}$$

Background:

$$P_{background} = 3.9504 \times 10^{-11}\ W \tag{1. 33}$$

$$N_{background} = 1.5265 \times 10^{9} s^{-1} \tag{1. 34}$$

Optical Throughput:

$$Throughput = 7.854 \times 10^{-13}\ m^2 \cdot sr \tag{1. 35}$$

Optical Noise:

$$NEP_{optics} = 1.0591 \times 10^{-15}\, W \tag{1.36}$$

Electrical Noise:

$$NEP_{electricity} = 3.9894 \times 10^{-8}\, W \tag{1.37}$$

Optical SNR:

$$SNR_{optics} = 0.7598 \tag{1.38}$$

Electrical SNR:

$$SNR_{electricity} = 2.0172 \times 10^{-8} \tag{1.39}$$

From the result above, we can conclude that the reason why the signal power is too weak is because the optical throughput is too small. And the reason why the throughput is so small is because the area of the object, where the small fluctuation of temperature happens, $A = 1\mu m \times 1\mu m = 1 \times 10^{-12} m^2$ is too small. In conventional infrared system, for example the infrared thermometer or infrared night vision scope, the source area of these appliances is as large as several centimeter squares to several meter squares. Therefore, how to detect such a weak signal in such a really small source area is the key issue to essentially realize infrared microscope.

On the other hand, from the result shown as above, the noise from the electrical detector $NEP_{electricity} \gg NEP_{optics} > \Delta P$. is extraordinarily larger than the signal. So the weak signal is drown in the sea of noise that the detector can capture nothing at all. And among these noises, the electrical noise introduced by the detector is the most crucial one needed to be controlled. Since the photon shot noise from the background is not so much larger than the signal, we can filter this noise by using lock-in amplifier or other low pass filters.

From the calculation above, we can conclude that the VML 10T0 photodiode cannot fulfill our requirement and no longer be used in this case. So, in order to deal with electrical noise, there are three other ways can be considered to take:

- Using optical amplifier to intensify the optical signal power
- Using more sensitive detector with low noise
- Using amplifier combining sensitive detector

The following chapters will further discuss these methods in detail.

Chapter 2. Optical Amplifier

An optical amplifier is a device that amplifies an optical signal directly without the need first convert to electrical signal and then amplifies it. An optical amplifier's principle is very similar to laser, so it can be thought of as a laser without an optical cavity. Optical amplifier is very important in optical communication and laser physics. There are several types of optical amplifiers, solid-state amplifier, erbium-doped optical fiber amplifier, semiconductor optical amplifier, Raman amplifier, optical parametric amplifier, gas laser amplifier, etc.

2.1 CO_2 Laser Amplifier

Transversely Excited Atmospheric (TEA) CO_2 laser amplifier is a kind of gas laser amplifier. The resonant wavelength is 10.6μm, which can be used in our design to amplify signal for the peak wavelength of the cell radiation is nearly 9μm-10μm. The pump of the laser amplifier is achieved by high voltage electrical discharge in a gas mixture at or above atmospheric pressure. CO_2 laser amplifier is a 4-level system. The process of population inversion mechanism is shown in figure *Figure 2. 1* [18].

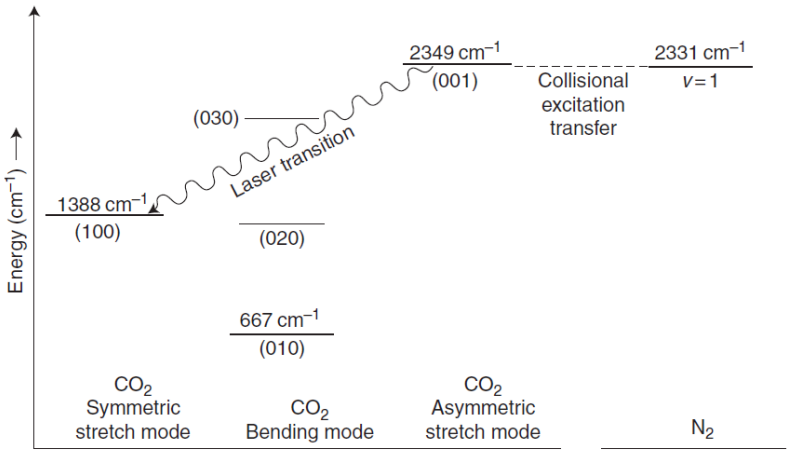

Figure 2. 1 CO_2 Laser Mechanism

The upper CO_2 laser level is pumped by excitation transfer from the nitrogen molecule, with N_2 itself excited by electron impact. The first excited vibrational level ($\upsilon = 1$) of the N_2 molecule lies close to the level (001) (one of)of CO_2. Because of this near resonance, there is a rapid excitation

transfer between $N_2(\upsilon = 1)$ and $CO_2(001)$. $N_2(\upsilon = 1)$ is itself a long-lived level, so it effectively stores energy for eventual transfer to $CO_2(001)$. Laser action in CO_2 lasers occurs on the vibrational transition $(001) \rightarrow (100)$ of CO_2. This transition has a wave number around $(2349 - 1388)\ cm^{-1} = 961\ cm^{-1}$ and this is a wavelength $(961\ cm^{-1})^{-1} = 10.4\mu m$ in infrared. The laser wavelength depends also on the rotational quantum numbers of the upper and lower laser levels. For the case in which the upper and lower levels are characterized by J= 19 and 20, respectively, the wavelength is about $10.6\mu m$, the most common CO_2 laser wavelength.

The (100) and (020) vibrational levels of CO_2 are essentially resonant. This "accidental degeneracy" results in a strong quantum coupling and these two states lose their identities. Furthermore the (020) and (010) levels undergo a very rapid vibration-to-vibration (VV) energy transfer

$$CO_2(020) + CO_2(000) \rightarrow CO_2(010) + CO_2(010) \qquad (2.\ 1)$$

The (010) level thus acts in effect like a lower laser level that must be rapidly "knocked out" in order to increase population inversion. Fortunately, it is relatively easy to deexcite the (010) level by vibration-to-translation (VT) processes:

$$CO_2(010) + A \rightarrow CO_2(000) + A \qquad (2.\ 2)$$

where A represents some collision partner, for example H_2, N_2 and CO_2. The VT deexcitation of (010) effectively depopulates the lower laser level and also puts CO_2 molecules in the ground level, where they can be pumped to the upper laser level by the VV excitation transfer

$$N_2(\upsilon = 1) + CO_2(000) \rightarrow N_2(\upsilon = 0) + CO_2(001) \qquad (2.\ 3)$$

Figure 2. 2 74[19] indicate a specific structure of CO_2 laser. The gain tube is 60cm long. The NaCl Brewster window is to give a linearly polarized output. With external output mirror, we can make this gain tube as CO_2 laser. If without the output mirror, this gain tube serves as CO_2 amplifier, and the signal light double pass this gain tube to get a double gain through this amplifier.

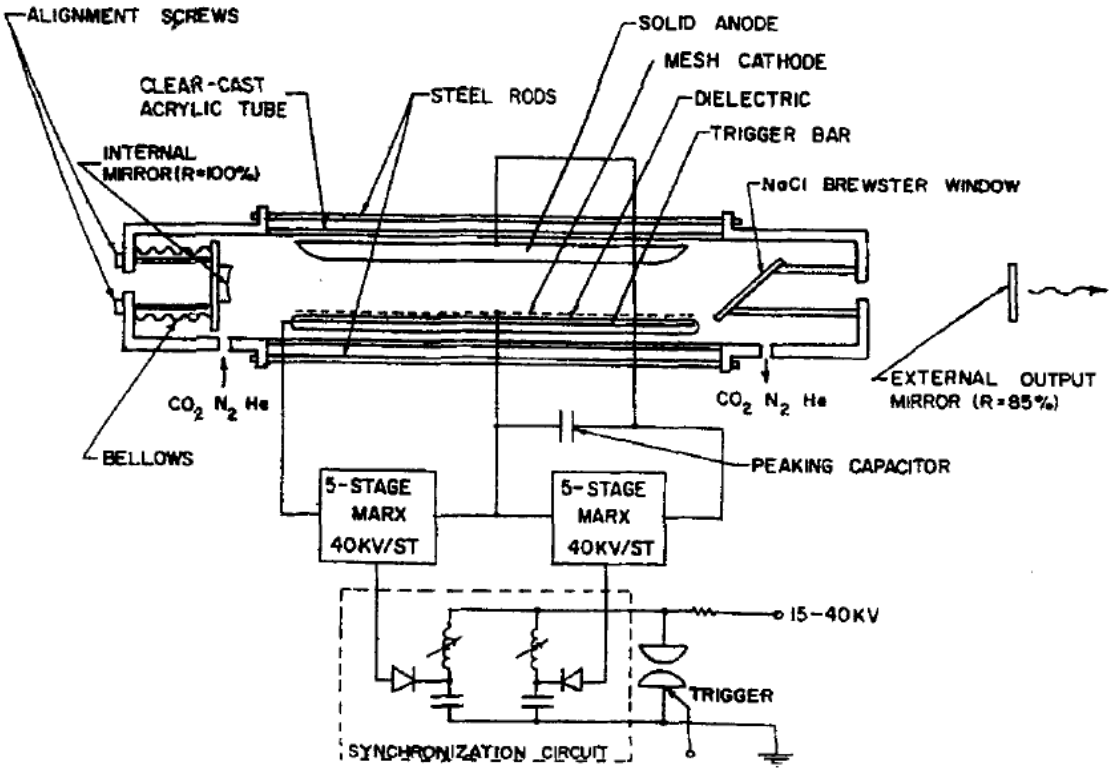

Figure 2. 2 CO_2 Laser Layout

2.2 Gain Analysis

We use a collimator lens to make the focus light becoming collimating beam coming through the CO_2 laser amplifier. The light power then can be amplified by the gain medium, in this case, the gain medium is gas medium -- CO_2 . The light power is amplified exponentially:

$$P_{out} = P_{in}e^{gL} \tag{2. 4}$$

Where g is the small signal gain of the CO_2 amplifier, L is the length of the gain medium. The typical small signal gain of CO_2 amplifier has a range from 0.02 to 0.05 cm^{-1} [20][21]. And the typical length of the gain medium has a range from 40 to 100cm [19][20][21]. So if we choose $g = 0.05\ cm^{-1},\ L = 100cm$. And define the gain coefficient $G = e^{gL}$, so the equation can be written as

$$P_{out} = GP_{in} \tag{2. 5}$$

With the data given above, we can calculate if the light pass one time, $G = 148$; if twice, $G \approx 2 \times 10^4$; if third, $G \approx 3 \times 10^6$. Remember that the signal power is 10^{-8} time smaller than the electrical noise. If we let the signal beam passing three times or more through the gain medium, the signal is getting closer to the electrical noise and if with lock-in amplifier,

we can again amplify signal electrically about 1000 times and at the same time this amplifier can filter out the electrical noise or making it faint. So in this optical amplifying way, we can amplify the signal directly without at the same time amplifying electrical noise.

The arrangement of the amplifiers can be cascade coupling, but if we put one after another, this will make the system really long as one amplifier has 1 meter long. So to make the system more compact and at the same time, decrease noise from the amplifier in each stage, we can arrange the amplifier with reflected prism/mirror as shown in *Figure 2. 3* .

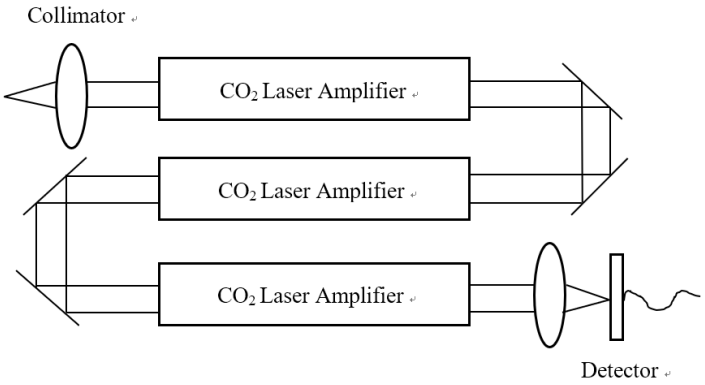

Figure 2. 3 Schematic of Cascade CO_2 Laser Amplifier Arrangement

In addition to this cascade coupling scheme, there's other schemes to get signal amplified, for example, regenerative ring amplifier *Figure 2. 4* [22]. This scheme is to arrange the reflective mirror/prism to let the light travel in a circle and to be amplified by the amplifier in each circle.

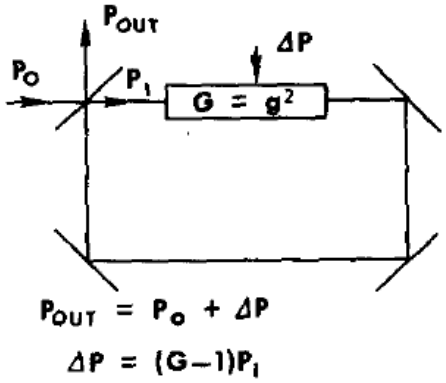

Figure 2. 4 Schematic of Regenerative Ring Amplifier

There are two operation modes in this arrangement. One is operating in unconditionally stable mode, in this mode, $G_0R < 1$ in all wavelengths, the cavity become unstable and cannot be lased, so the power inside the cavity will be amplified and then be extracted from the cavity.

Another mode is operating in conditionally stable mode, in this mode, first $G_0R > 1$, the ring become stable. However, the amplifier will be saturated and the gain G will decrease making $GR < 1$. Then the power inside the cavity can then be extracted again. Although this scheme is much more compact, but the amplified gain is not as much as cascade coupling, the gain can achieve about 1000 times or more. This is because the gain is closely dependent on the reflectivity of the mirror, if the reflectivity is higher, the power can be amplified more, but we can only extract less power, if the reflectivity is lower, we can extract more power, but the signal may not be enough amplified. So the reflectivity can only be chosen the optimal one, that makes the amplified gain cannot be larger. But in cascade coupling, the signal can not be infinitely amplified either, because the amplifier will get saturated if the signal is large enough and the gain will decrease too. However, the saturation irradiance is about $10W/cm^2 \sim 100W/cm^2$ with collision cross section value and 001 CO_2 laser level lifetime value provided [23]. Compared to the background irradiance $100nW/cm^2$, the saturation irradiance is extraordinarily larger, so during the first several stages, we can ignore the saturation effect in cascade coupling mode.

There's another regenerative scheme, which is simpler than ring regenerative amplifier, called Fabry-Perot regenerative amplifier *Figure 2. 5* [22]. As we can conclude that we don't necessarily need to arrange in ring amplifying structure. The reason why they arranged in ring structure was because in Fabry-Perot regenerative amplifier, the oscillator is in line with the amplifier that can reflect power back toward the stable laser to cause deleterious frequency changes which would compromise the frequency stability of the system. So they use nonreciprocal isolator to prevent this situation. But in ring arrangement, no power can be directed back to the master oscillator from the amplifier to cause deleterious frequency changes.

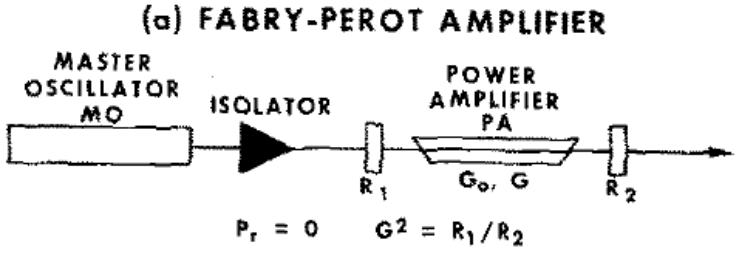

Figure 2. 5 Schematic of Fabry Perot Regenerative Amplifier

But in our case, there's no worry about the backward power, so both these technologies can be used in our design. In Fabry-Perot amplifier, the power we get from the amplifier has close relationship with two mirror's reflectivity. But as we can see in Fabry-Perot amplifier

arrangement, there's some power leakage in the first mirror. So this arrangement efficiency is not as high as ring regenerative amplifier.

By considering these three schemes, cascade coupling amplifier is more suitable in our high gain requirement design.

2.3 Noise Analysis of Laser Amplifier

2.3.1 Noise Expression of Laser Amplifier

The noise model of amplifier have been solved by H.Kogelnik and A.Yariv 75[24]. They indicate that the noise added to the signal after being amplified by the amplifier is coming from the spontaneous emission of atoms in the upper laser level.

The model of noise can be represented simply in *Figure 2. 6* . The expression for power gain can be obtained from Yariv and Gordon [25].

$$\gamma(v) = \frac{\left(n_2 - n_1\frac{g_2}{g_1}\right)c^2 g(v)}{8\pi v^2 t_{spont}} \qquad (2.\ 6)$$

Where g_1 and g_2 are the degeneracies of the two laser levels, c is the velocity of light, t_{spont} the spontaneous emission lifetime for 2 → 1 transition and $g(v)$ the atomic line shape function.

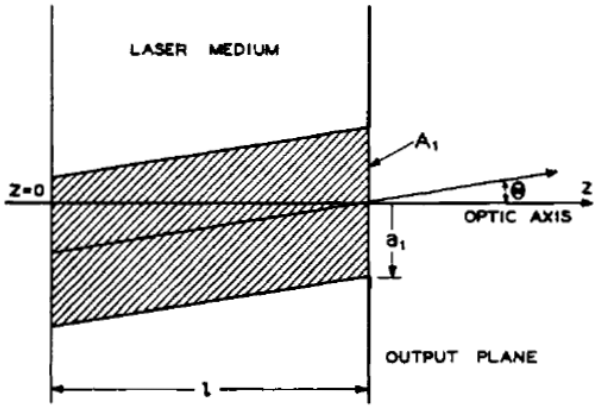

Figure 2. 6 Noise Model in the Gain Medium

In *Figure 2. 6*, there's an aperture stop in output plane with a round hole of radius a_1 and area $A_1 = a_1^2\pi$ to provide for passage of the signal. In a small volume dV of the medium with a density n_2 of excited states, the amount of noise power at frequencies between v and $v + dv$ radiated into a solid angle $d\Omega$ is

$$dN = hv\frac{n_2 g(v)}{t_{spont}}\frac{d\Omega}{4\pi}dvdV \quad (2.\ 7)$$

The noise emitted at a coordinate z and propagating at an angle θ with respect to the z axis is amplified by a factor $e^{\gamma(l-z)/cos\theta}$ until it reaches the output hole or is intercepted by the screen. For a given θ and a polar angle ϕ, only noise originating from within the shaded cylinder shown in *Figure 2. 6* can escape through the output hole. If we sum the contributions of all volume elements within the cylinder and take account of the proper amplification factor, we obtain the noise power $N(\theta)$ radiated through the hole A_1 at an angle θ into $d\Omega$:

$$N(\theta) = A_1 \int_0^l dz \cdot \frac{dN}{dV} \cdot e^{\gamma(l-z)/cos\theta} \quad (2.\ 8)$$

The evaluation of this integral yields

$$N(\theta) = A_1 cos\theta \frac{[G(\theta)-1]}{\gamma}\frac{hvn_2 g(v)}{t_{spont}}\frac{d\Omega}{4\pi}dv \quad (2.\ 9)$$

Where we have defined the gain $G(\theta)$ of the amplifier as

$$G(\theta) = e^{\gamma l/cos\theta} \quad (2.\ 10)$$

Substituting the expression for γ from (2. 6) we arrive finally at

$$N(\theta) = 2hvdv\frac{n_2}{n_2 - n_1\frac{g_2}{g_1}}(G-1)\frac{A_1 cos\theta d\Omega}{\lambda^2} \quad (2.\ 11)$$

Where λ is the wavelength. We obtained a law of noise radiation which is very similar to the law of black-body radiation. We also define the amount of "noise per mode" as N_0:

$$N_0 = 2hvdv\frac{n_2}{n_2 - n_1\frac{g_2}{g_1}}(G-1) \quad (2.\ 12)$$

So the total amount of noise escaping through the aperture stop can be obtained by integrating over all-solid angles, the result is:

$$N_{tot} = N_0\frac{\pi A_1}{\lambda^2} \quad (2.\ 13)$$

If the noise power emitted into a cone of very small apex angle θ, we can approximate $\Omega = \pi sin^2\theta \approx \pi\theta^2$ and the noise power can be expressed as:

$$N_\Omega = N_0\frac{A_1\Omega}{\lambda^2} \quad (2.\ 14)$$

The total amount of noise N_{tot} is a special case of N_Ω. If $\theta = \frac{\pi}{2}$, which is a large angle, we cannot use solid angle approximation and the exact value of solid angle can be express as $\Omega = \pi sin^2\theta = \pi$, substitute it into (2. 14), we can get (2. 13). (2. 14) can be used to approximate the noise coming from a long tube amplifier with very thin laser gain medium, because in most cases, the noise model of H.Kogelnik is inconsistent with the reality since

there are no infinitely large bulk-like laser medium. Laser gain medium always have finite edge and sometimes the thickness of gain medium cannot be extended so large, for example, thickness of gain medium of the quantum well laser is very thin. So, in reality, (2. 14) provide a way to approximate the noise in a thin tube-like laser medium by using a solid angle exited from the output aperture to entrance aperture of the laser medium like *Figure 2. 7* shown.

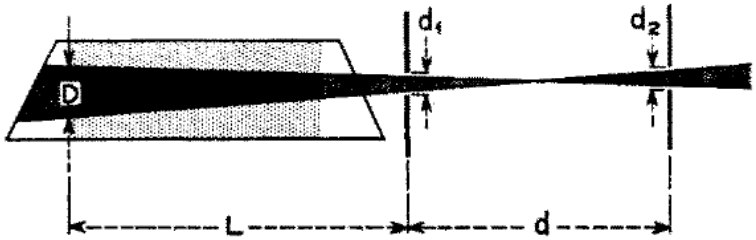

Figure 2. 7 The Throughput (black cone) of a Laser Medium Modulated by Two Apertures

If we approximate solid angle as $\Omega \approx \frac{A_2}{l^2}$, where A_2 is the area of entrance aperture, l is the length of the gain tube, we can find that the term $A_1\Omega = \frac{A_1 \times A_2}{l^2}$ is the inherent throughput of the laser gain tube. So we can also simplify (2. 14) as:

$$N_\Omega = \frac{N_0}{\lambda^2} \times throughput \qquad (2.\ 15)$$

Where throughput is the inherent throughput of laser gain tube $throughput = A_1\Omega = \frac{A_1 \times A_2}{l^2}$. But actually, if the system's throughput is less than the throughput of laser gain tube, the throughput value in (2. 15) will transfer to system's throughput since the noise outside the system's throughput will not get into the system and can be ignore. And we can generalize the radiance of noise coming out from the laser is $L = \frac{N_0}{\lambda^2}$. This property can be used to analyze the propagating behavior of the noise coming out from the laser so that we can control the amplifier's noise.

2.3.2 Noise Reduction 75[24]

Consider a signal beam with a Gaussian transverse field distribution and a minimum beam radius(spot size) of a_m. The output screen is aperture in front of the detector, if the aperture can fulfill the minimum beam radius of a_m, it means that all the signal can be accepted by the detector(in reality, this is not true for there's upper mode and there's ray propagating outside the beam waist, but the beam waist is a good approximation of most power of the signal).

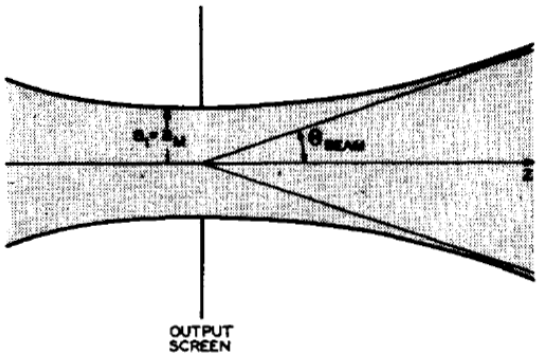

Figure 2. 8 Beam Collection: The aperture constrained to the Gaussian Beam pattern cannot collect all the power going through due to higher modes being blocked, but it is good criteria to collect most of the power

So we set a lens close to the output plane of the laser to focus signal light into focal plane as shown in *Figure 2. 9* .

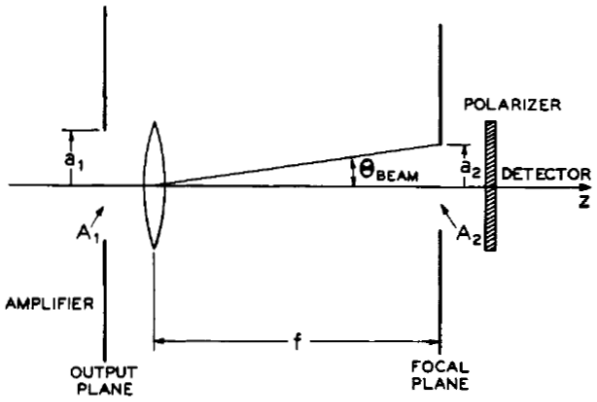

Figure 2. 9 Noise Reduction Setup

The focal plane is opened with the radius $a_2 = a_m$. The noise-reduction setup shown in *Figure 2. 9* is basically suggested by Schawlow and Townes [26]. In this structure, the purpose is to make $\frac{A_1\Omega}{\lambda^2} = 1$, so the noise of the system equals to N_0. And at the same time, throughput of the laser compromise to the system throughput. So in the end, the focal length of the lens f should satisfy the condition:

$$\frac{A_1 \times A_2}{f^2\lambda^2} = 1 \qquad (2.\ 16)$$

Where $A_1 = \pi a_1^2,\ A_2 = \pi a_m^2$. Then in this condition, the signal to noise of amplifier is

$$SNR_{amplifier} = S_0/N_0 \qquad (2.\ 17)$$

To design the interval space between each amplifier, we can use (2. 15). Since the cascade coupling scheme need to direct light into each amplifier with prism reflection shown in *Figure 2. 3* , we can unfold each light path to make it a general case shown in *Figure 2. 10* .

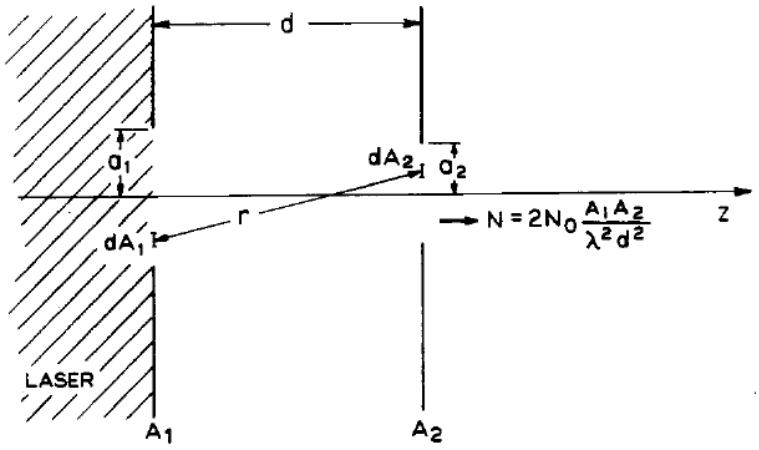

Figure 2. 10 Two Aperture Coupling in General Case After Laser Medium

In (2. 15), the throughput between two aperture can be express as

$$throughput = \frac{A_1 \times A_2}{d^2} \tag{2. 18}$$

So the noise propagating through this interval space is

$$N = N_0 \frac{A_1 \times A_2}{\lambda^2 d^2} \tag{2. 19}$$

We define a parameter α:

$$\alpha = \frac{A_1 \times A_2}{\lambda^2 d^2} \tag{2. 20}$$

This parameter is called acceptance factor. Using this parameter, (2. 19) becomes

$$N = N_0 \alpha \tag{2. 21}$$

Which is really a really simple form to analyze the noise of amplifier. As we can find that in the case of detector imaging space, the acceptance factor $\alpha_{detector} = 1$. To make the noise as small as possible we need to reduce each acceptance factor in each stage of amplifier as small as possible but at the same time ensuring the signal can go through the system as much as possible.

2.3.3 The Relationship Between Blackbody Radiation and Spontaneous Noise

From the previous section, we know the blackbody radiation is expressed in the form of (1. 1)

$$Md\lambda = \frac{2\pi hc^2}{\lambda^5 (e^{\frac{hc}{\lambda k_B T}} - 1)} d\lambda$$

With $d\lambda = \frac{\lambda^2}{c} dv$, and radiance expression $L = M/\pi$, combining $P = L \times throughput$, the blackbody radiation can be expressed as

$$Pdv = \frac{2hvdv}{\frac{hc}{(e^{\overline{\lambda k_B T}} - 1)}} \cdot \frac{throughput}{\lambda^2} \tag{2. 22}$$

Compared to spontaneous noise expression:

$$N_\Omega dv = \frac{N_0}{\lambda^2} \times throughput = 2hvdv \frac{n_2}{n_2 - n_1 \frac{g_2}{g_1}} (G - 1) \cdot \frac{throughput}{\lambda^2} \tag{2. 23}$$

Where throughput is the system throughput(assuming the inherent throughput of the gain medium is larger than the system throughput).If we define the noise equivalent power NEP before the noise being amplified by the amplifier, which is a numerical power that do not exist, but it is convenient to analyze in this issue.

$$NEPdv = \frac{N_\Omega dv}{G} = 2hvdv \frac{n_2}{n_2 - n_1 \frac{g_2}{g_1}} \frac{(G-1)}{G} \cdot \frac{throughput}{\lambda^2} \tag{2. 24}$$

If $G \gg 1$, the expression can be simplified into

$$NEPdv = 2hvdv \frac{n_2}{n_2 - n_1 \frac{g_2}{g_1}} \cdot \frac{throughput}{\lambda^2} \tag{2. 25}$$

Actually, blackbody radiation is a special case of (2. 25)[24]. We recall that the excited states inside of a black box are in equilibrium. That means that the population densities are such that

$$\frac{n_1/g_1}{n_2/g_2} = e^{hv/k_B T} \tag{2. 26}$$

Substitute this expression into (2. 25). Then we can obtain (2. 22) (note that γ is negative for positive T, and since the power is always positive, so we change sign here).

If we assume that, $g_1 = g_2$, $n_2 \gg n_1$, this condition is very common in most of the 4-level laser. Then (2. 25) becomes

$$NEPdv \approx 2hvdv \cdot \frac{throughput}{\lambda^2} \tag{2. 27}$$

Then the signal to noise ratio between blackbody radiation and the equivalent noise power can be calculated:

$$SNR_{amplifier} = \frac{P}{NEP} = \frac{1}{\frac{hc}{(e^{\overline{\lambda k_B T}} - 1)}} \approx 0.01 < 1 \tag{2. 28}$$

Unfortunately, this means that if we take blackbody radiation as a signal to be detected. It is impossible to use one-stage laser gain medium to amplify the signal because the spontaneous noise will be added and it is constantly larger than the blackbody radiation signal.

However, if one stage cannot be realized, we can use multiple stages by using cascade coupling as mentioned before. Because, we can control the throughput/acceptance factor of the noise in each stage to reduce noise without affecting the system throughput. That means we need to control $Throughput_{noise} < Throughput_{signal}$ to further reduce noise power.

2.4 Quantum Cascade Laser Amplifier

The other method to avoid this limitation is to use amplifier gain medium of quantum cascade laser. Quantum cascade laser can be tailored to cover most of the infrared spectrum to Terahertz spectrum, for example with emission wavelength from $2\mu m$ to $100\mu m$. So it can be used to amplify infrared signal in our design. The reason why quantum cascade laser can work is because the excited electron can radiate multiple photons instead of just one photon in many typical laser amplifiers. And the stimulated photons are produced more with the increase of injection current density.

In the typical 4-level system laser, the population inversion is determined by the formula below:

$$\Delta N = n_2 - n_1 = \frac{P}{A_{spont}+P} N_T \tag{2. 29}$$

Where n_2, n_1 are the population density in excited state and depopulation level, P is the pumping rate, A_{spont} is the spontaneous emission rate, N_T is the total population density inside the gain medium. If $P \gg A_{spont}$, $\Delta N \approx n_2 = N_T$, this is the condition we have discussed in (2. 27).

But in the quantum cascade laser, even though every stage in this laser's active region acts as 4-level system, there are multiple stages arranged in cascade coupling in the quantum cascade laser active region. So the rate equations in quantum cascade laser are different from traditional 4-level laser system's rate equations. This mechanism leads to different gain expression of the laser gain medium [27]

$$\gamma = g\Gamma_p N_p J \tag{2. 30}$$

Where Γ_p is the overlap factor between the mode and one periodic stage of the structure, N_p is the number of periods or number of the stages, g is gain coefficient for the case of comparable lifetime τ_3(excited level's lifetime) and τ_2(depopulation level's lifetime):

$$g = \frac{4\pi q}{\epsilon_0 n}\frac{(\tau_{32}-\tau_2)(\tau_3/\tau_{32})}{2\gamma_{32}L_P}\frac{(z_{32})^2}{\lambda} \quad (2.\ 31)$$

Where q is the charge density, ϵ_0 is vacuum permittivity, n is the mode refractive index, γ_{32} is the FWHM of the luminescence, L_P is the length of each stage, λ is the emission wavelength, z_{32} is the transition matrix element, τ_{32} is the intersubband scattering time. All of the factors g, Γ_p, N_p are constant, so the gain of the laser is proportional to current density shown in *Figure 2. 11* :

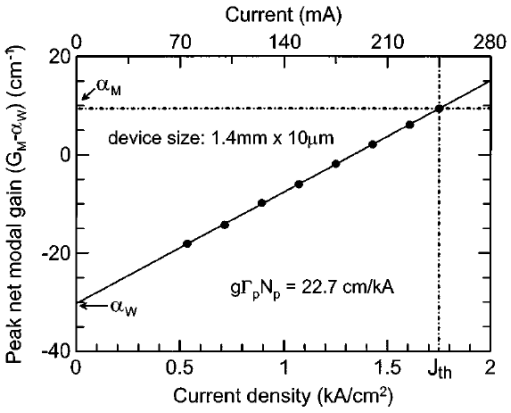

Figure 2. 11 Proportional Relation between Gain and Current Density

So if we substitute (2. 30) into (2. 9) , after doing integration and calculating the noise equivalent power as the same method as (2. 25) , we can have the relationship $NEP \propto 1/J$. Therefore, the signal to noise ratio have the relationship

$$SNR_{amplifier} = \frac{P}{NEP} \propto \frac{J}{(e^{\frac{hc}{\lambda k_B T}}-1)} \quad (2.\ 32)$$

In this case, we can adjust the injection current density J to increase the signal to noise ratio so that we can have signal be detected and recognized.

Chapter 3. Other Sensitive Detectors

Since we have serious problems in using optical amplifier because of the spontaneous noise introduced by amplifier itself interfering the original blackbody radiated signal, we need the other approaches to detect this faint signal. Although we have mentioned that quantum cascade laser can be used to amplifying the signal, this approach may not be assured enough to make the signal be detected because the method is too limited that we can increase the signal to noise ratio just by only increasing the current density. So in order to guarantee and prove the possibility that the signal can be detected, we need other alternative assisted methods.

In addition to optical amplifier, we can use more sensitive detector instead of VML10T0 photodiode. Also, in addition to photodiode detector, we still have many common types of infrared or thermal detectors, for example, thermocouple, thermopile, bolometer, pyroelectric, photoconductive detector. But these types' detector so far may not satisfy our design requirement, for the best pyroelectric, the detectivity can only reach to $5 \times 10^9 cm \cdot Hz^{\frac{1}{2}}/W$. There are also many types of photoconductive detector, whose detectivities are shown in *Figure 3. 1* , but no such one can satisfy our requirement for at least $10^{12} \sim 10^{13} cm \cdot Hz^{\frac{1}{2}}/W$. The microbolometer's theoretical noise equivalent temperature difference (NETD) can reach to 0.01K, but as for our expectation, we need temperature resolution to be 0.001K. Although maybe in the end, in our design, we cannot reach to a resolution of 0.001K, we still want to pursue for detector with higher sensitivity to make our goal seems like possible and feasible.

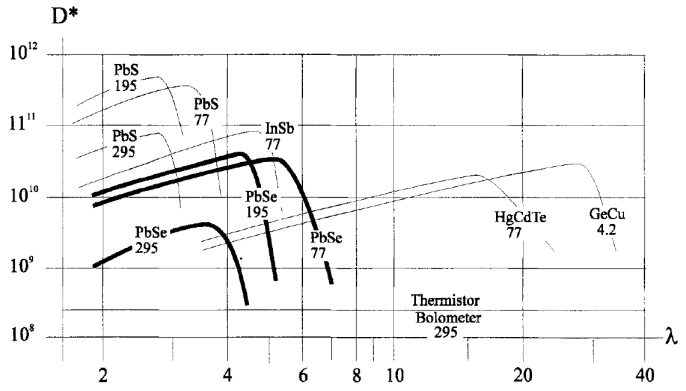

Figure 3. 1 Detectivity of Some Photoconductive Detector

There are multiple sensitive detectors nowadays, for example, avalanche photodiode (APD), superconducting nanowire single-photon detector (SNSPD), quantum well infrared photodetector (QWIP), quantum dot infrared photodetector (QDIP), microchannel plate detector (MCP), photomultiplier tube (PMT), HgCdTe detector.

3.1 Superconducting Nanowire Single-Photon Detectors

Superconducting nanowire single-photon detector (SNSPD) is invented based on Cooper pairs in superconducting condition. And it is constructed with current-biased super superconducting nanowire. It is very sensitive that can be used for photon counting. But most of SNSPD can only be used in near-infrared spectrum. Compared to our blackbody's peak wavelength lying in LWIR, this spectrum is not a good choice for detection. The typical NbN nanowire SNSPDs can reach a detection efficiency about 30% and sometimes can even go higher to 67% at 1064nm wavelength [28]. But most of the SNSPDs' efficiency drop considerably for wavelength above $1\mu m$. Even though efforts have been made to extend the infrared spectrum of SNSPDs for example by using NbSi nanowire to detect a wavelength up to $1.9\mu m$[29], this is still far from our expectation of about $10\mu m$. In addition, SNSPD needs the superconducting condition always working in a critical temperature below 10K. This will undoubtedly increase the expense of the microscope by using advanced cooling method.

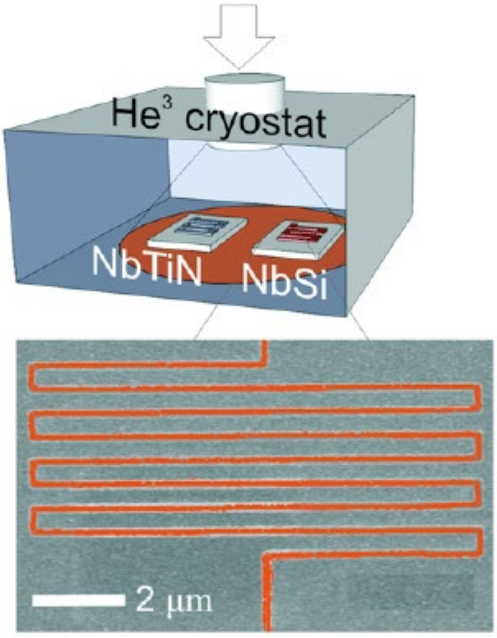

Figure 3. 2 NbTiN & NbSi Superconducting Nanowire Single Photon Detector (Above) and Nano wire thereof (Bottom)

3.2 Microchannel Plate and Photomultiplier Tube

Microchannel plate (MCP) is always used in combination of photomultiplier tube (PMT). This kind of detector is called MCP-PMT detector.

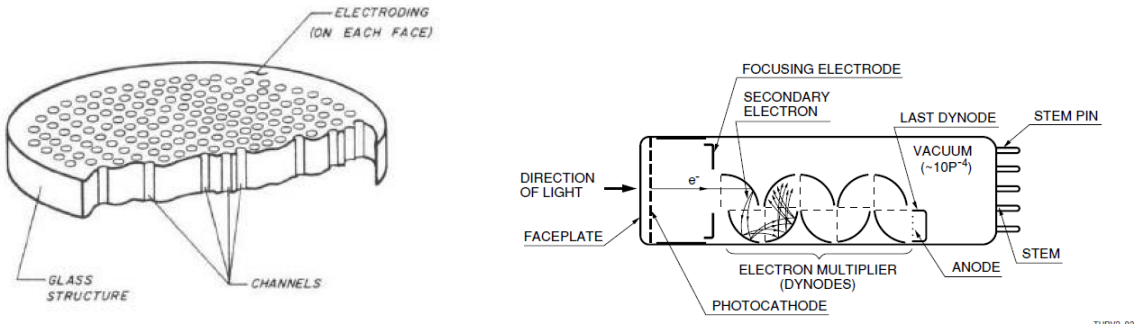

(a) (b)

Figure 3. 3 Microchannel Plate(MCP) & Photomultiplier Tube (PMT): (a) Microchannel Plate(MCP) (b) Photomultiplier Tube (PMT), sometimes we combine both of these into MCP-PMT detector.

The advantage of this detector is that it can provide a really high gain of $10^4 \sim 10^7$ with really low noise. This detector has been used to diagnose CMOS circuit from the backside where picosecond pulses of light emitted from the circuit can be detected in a window of near-infrared wavelength range($0.9\mu m \sim 1.4\mu m$) [30]. However, this detector is based on photoelectric effect. As we can suppose, if we want to excite a escaping electron, we need relatively high energy photon. For this reason, the detection wavelength cannot be too long to cover even MWIR, never to say LWIR. And this is why the most common Ag-O-Cs photocathode have working wavelength from $300nm \sim 1200nm$. Higher wavelength sensitive photocathode has been reported [31] to $1.35\mu m$ by using InP/InGaAsP and Hamamatsu claimed that they have produced commercial InP/InGaAsP photocathode extending to $1.4\mu m$ or even $1.7\mu m$ [32]. This is right now the highest wavelength sensitive photocathode reported having been made. However, even higher wavelength sensitive photocathode from $0.9\mu m\ to\ 10\mu m$ has been theoretically claimed [33]. What they do is to combine GaSb($\sim 1.7\mu m$), InAs(~$4\mu m$) and InAs/GaInAlSb superlattice($1.7\mu m \sim 10\mu m$) as photons absorbing layer, which can absorb $0.9\mu m\ to\ 10\mu m$ IR photons to excite electrons to the conduction band of absorbing layer, then apply external electric field to transport these electrons into conduction band of GaAlSb layer, in which these electrons can be ejected into vacuum to form a special photocathode as a whole. This seems reasonable to get a higher wavelength sensitive photodiode, but this patent just discussed only about an invention, an experimental prototype or even the experimental testing figure has not been shown in this patent. So by now, we can only conclude that the highest working wavelength of MCP-PMT is up to $1.7\mu m$. This type of detector is not suitable in our design.

3.3 Intersubbands Infrared Photodetectors

Quantum dot infrared photodetector (QDIP) or quantum well infrared photodetector (QWIP) are based on the effect of intersubband transition of photoelectrons. These intersubband are formed by quantum confinement to make the band discrete in the conduction band. These intersubbands transitions absorb less energy than interband transition because they have less band gap than the band gap between conduction band and valence band. So these devices can be used to detect infrared photons.

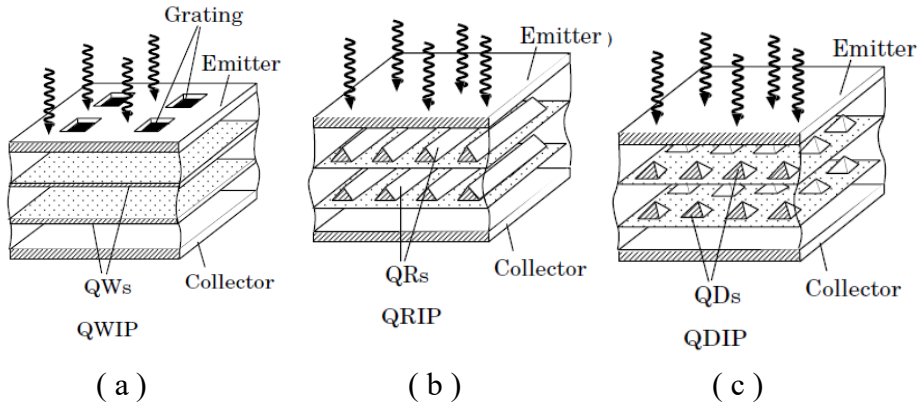

Figure 3. 4 Several Types of Intersubbands Infrared Photodetectors Structure: (a) Quantum well infrared photodetector (QWIP) (b) Quantum rod infrared photodetector (QRIP) (c) Quantum dot infrared photodetector (QDIP)

There is also another type of intersubbands detector, called quantum wire infrared photodetector (QRIP). The difference between these detectors is that quantum effect are confined in different dimension, quantum well is confined in one dimension, quantum wire is confined in two dimensions, quantum dot is confined in three dimensions. The characteristics of these detectors has been analyzed [34], due to dipole selection rules, IR photons polarized laterally in the QW plane is forbidden in QWIPs, but this is not a problem in QRIPs and QDIPs for they can be realized with lateral confinement, so QRIPs and QDIPs have higher responsivity than QWIPs but at the same time with higher gain, have higher dark current amplified by higher gain. QRIPs and QDIPs are inferior to QWIPs in detectivity. But if we increase the density of narrow QRs and QDs array, the QDIPs and QRIPs can theoretically [34]surpass QWIPs in detectivity. Although in calculation, QWIPs detectivity in $\lambda = 10.7\mu m$ can increase from $10^{10} cm \cdot Hz^{\frac{1}{2}}/W$ at $77K$ to $10^{13} cm \cdot Hz^{\frac{1}{2}}/W$ at $35K$ [35], normal incidence quantum efficiency of $\eta = 28\%$, and detectivity of $D^* = 3.1 \times 10^{10} cm \cdot Hz^{\frac{1}{2}}/W$ at $77K$ with GaAs/AlGaAs QWIP for a cutoff wavelength $\lambda = 7.9\mu m$ was reported being realized [36]. Although in calculation, detectivity in QDIP with high density assemble can be higher than QWIP—at $66K$, detectivity of $D^* = 10^{13} cm \cdot Hz^{\frac{1}{2}}/W$ in a detection

wavelength $\lambda = 10\mu m$ shown in *Figure 3. 5* [37], The actual reported experiment realized InAs-InGaAs QDIP with detectivity $D^* = 1.7 \times 10^9 cm \cdot Hz^{\frac{1}{2}}/W$ operating at $77K$ and $D^* = 9.0 \times 10^7 cm \cdot Hz^{\frac{1}{2}}/W$ at $150K$ detected at the peak wavelength of $11.7\mu m$ [38]. So, QWIPs and QDIPs are potential to be used in our design in a requirement of detectivity at least $D^* = 10^{12} \sim 10^{13} cm \cdot Hz^{\frac{1}{2}}/W$. But right now, the technology has not been advanced to the theoretical expectation so that we still need to consider other types of detectors.

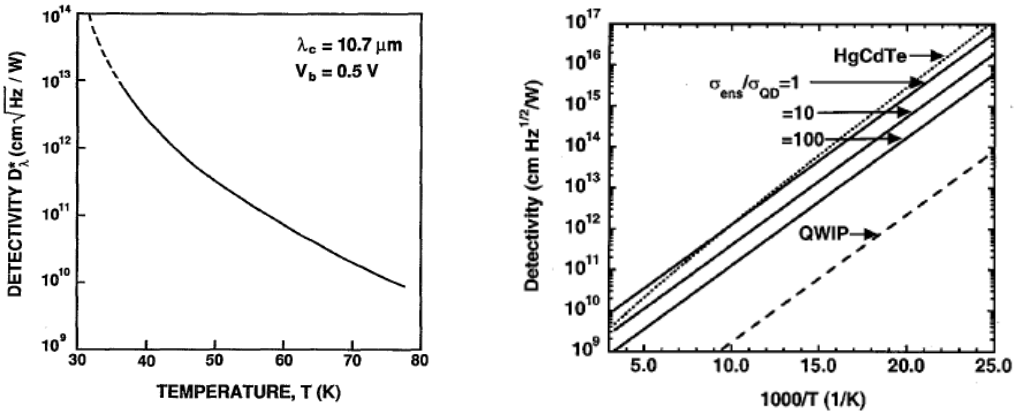

(a) (b)

Figure 3. 5 Detectivity of the QWIP and QDIP versus temperature: (a) QWIP theoretical detectivity versus temperature (b) Comparison of the detectivity of QDIP(solid line), QWIP(dash line), and HgCdTe PD(dot line), for QDIP, σ_{ens}/σ_{QD} is the absorption coefficient, the higher absorption coefficient, the lower percentage energy be absorbed by the quantum dot.

3.4 HgCdTe Detectors

In our design, the most suitable detector are HgCdTe based avalanche photodiodes(HgCdTe APD) or HgCdTe photodiodes(HgCdTe PD) . HgCdTe is very common material used in infrared detector. HgCdTe is an alloy of CdTe and HgTe with tunable bandgap spanning the shortwave infrared to the very long wave infrared regions. The amount of Cd in the alloy can be chosen so as to tune the optical absorption of the material to the desired infrared wavelength. CdTe is a semiconductor with a bandgap of approximately $1.5eV$ at room temperature. HgTe is a semimetal, which means that its bandgap energy is zero. Mixing these two substances allows one to obtain any bandgap between 0 to $1.5eV$, which means the sensitive wavelength theoretically can be $\lambda > 0.8\mu m$.

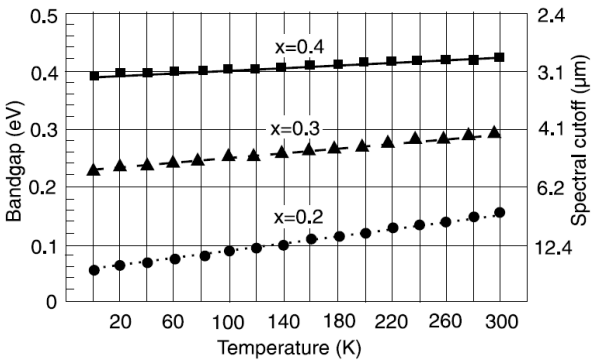

Figure 3. 6 Bandgap of the $Hg_{1-x}Cd_xTe$: Bandgap and corresponding spectral cutoff for representative alloy compositions of $Hg_{1-x}Cd_xTe$ as a function of temperature as calculated, x represents the proportion of the Cd in the alloy [39].

HgCdTe needs to be cooled near that of liquid nitrogen($77K$) to reduce noise due to thermally excited current carriers. There are also other alternative types infrared detector, for example, uncooled Si-based bolometers, InSb and photon-counting superconducting tunnel junction arrays, quantum well infrared photodetector. But these types of detectors are not as sensitive as HgCdTe detectors. HgCdTe detector also has very high quantum efficiency sometimes up to 90% with antireflection coating [39].

3.4.1 HgCdTe Photodiodes

HgCdTe photodiode (HgCdTe PD) is also a very excellent detector, the characteristics of this device can be shown in [39] The specific detectivity in *Figure 3. 9* can be evaluated in terms of relative noise levels present in the device.

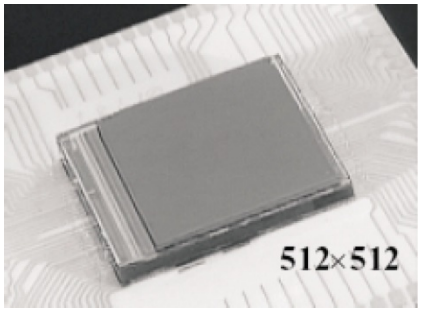

Figure 3. 7 HgCdTe Photodiode

The expression of detectivity can be given by the expression:

$$D^* = \frac{\eta q \sqrt{R_0 A}}{2h\nu\sqrt{kT}} \quad (3.\ 1)$$

Where η is the quantum efficiency, q is the electronic charge, $h\nu$ is the energy of the photon, and k is Boltzmann's constant, R_0A is the zero-bias dynamic resistance area product. R_0A represents the quality of HgCdTe photodiodes, which can be measured by leakage current shown in *Figure 3. 8* . With *Figure 3. 6*, we can find in *Figure 3. 8* that LWIR photodiode with $x = 0.213$, has a resistance area product $R_0A = 10^2\Omega \cdot cm^2$ at about $80K$, and MWIR photodiode with $x = 0.3$, the resistance area $R_0A = 10^7\Omega \cdot cm^2$ at about $80K$.

With $T = 80K$, $\eta = 0.8$. We can calculate detectivity for LWIR HgCdTe PD is $D^* = 1.16 \times 10^{12} cm \cdot Hz^{\frac{1}{2}}/W$, detectivity for MWIR HgCdTe PD is $D^* = 1.5 \times 10^{14} cm \cdot Hz^{\frac{1}{2}}/W$. In *Figure 3. 9* shows the detectivity vs resistance area product relationship of HgCdTe PD. If we have photodiode square pixel size $50\mu m$ and a bandwidth $\Delta f = 60Hz$, then for LWIR HgCdTe PD, by using the detectivity calculated above, we can get the noise equivalent power $NEP = 3.87 \times 10^{-16} W$, which is very near to signal power $\Delta P = 8.0474 \times 10^{-16}\, W$ in our design. Assume the responsivity of the detector is 1, then the electrical signal to noise ratio can be:

$$SNR_{electricity} = \frac{\Delta P}{NEP} = 2.08 > 1 \qquad (3.\ 2)$$

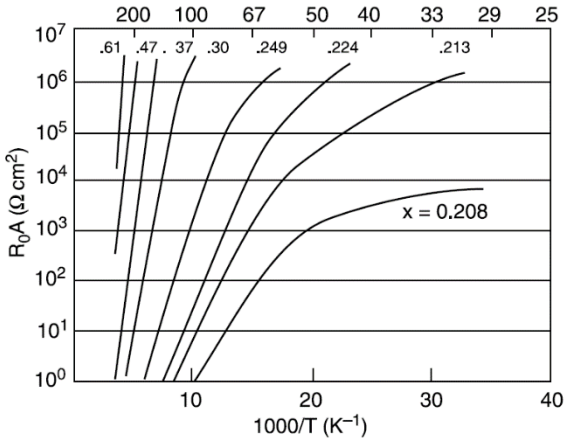

Figure 3. 8 Resistance Area Product R_0A as a function of temperature and x proportion of Cd in HgCdTe PD

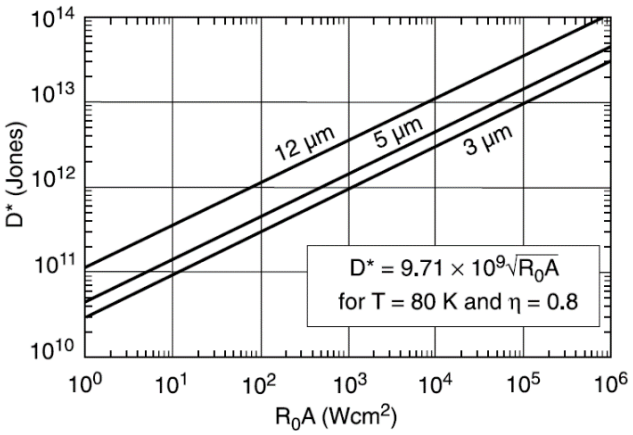

Figure 3. 9 The relationship between Detectivity and Resistance Area Product R_0A in HgCdTe PD

That means the detector right now can recognize the signal. Even if the responsivity of the HgCdTe PD is too ideal in the calculation, but for HgCdTe device with high quantum efficiency, $SNR_{electricity}$ will not degrade too much in real case.

Though LWIR devices are more difficult to produce than MWIR and SWIR devices, a decade ago, the technology was established to begin production of tactical long wavelength($10\mu m$) arrays with R_0A on the order of $10 - 100\Omega \cdot cm^2$. Nowadays, such devices are very common with high yield.

3.4.2 HgCdTe Avalanche Photodiodes

Avanlanche photodiodes(APD) based on HgCdTe is another option in our design. The

advantage of HgCdTe APD is that it has a very good high gain, about 5×10^3, but at the same time it will increase dark current. So dark current analysis is important in using this device.

With the help of APD noise model first proposed by R.J. McIntyre [40], we can evaluate APD multiplication gain as:

$$M(x) = \frac{G(x)}{1-\int_0^{\omega} \alpha(x)G(x)dx} \tag{3. 3}$$

$$G(x) = \exp\left[-\int_x^{\omega} \alpha(x') - \beta(x')dx'\right] \tag{3. 4}$$

Where 0 and ω are the two boundary surfaces of the photodiode, where $\alpha(x)$ and $\beta(x)$ are the electrons and holes' ionization probabilities per unit length, which are functions of only the electric field E.

The current shot noise spectral density $i_N(A/Hz^{1/2})$ in the output side of APD can be given by:

$$i_N = \sqrt{2qI_{in}M^2F} \tag{3. 5}$$

Where q is the electronic charge, M is the APD gain, I_{in} is the thermally and optically generated currents injecting into either end of the depletion layer of the APD, F is the excess noise factor which can be expressed as [43]:

$$F = \left[2 + \frac{1}{M(x)}\left(2\int_0^{\omega} dx'\alpha M^2(x') - M^2(\omega)\right)\right] \tag{3. 6}$$

Actually, this is the excess noise factor in the local-field theory proposed by R.J. McIntyre [40], there is also another model called history-dependent theory also proposed by R.J. McIntyre [44], which is used to deal with APD with short/thin multiplication length. In these APDs, nonlocal effects become significant, and the ionization coefficients are on longer the only functions of the local electric field. So in this theory, the excess factor expression looks different from the (3. 6). But in most cases, local-field theory is still a good model to describe the behavior of APDs, so in this paper, we still focus more on local-field theory.
In local-field theory, if the ionization coefficients satisfy simple linear relationship $\beta = k\alpha$, which means electron and hole ionization coefficients vary in roughly the same manner with electric field. The excess factor can be simplified to [40]:

$$F = M\left[1 - (1-k)\left(\frac{M-1}{M}\right)^2\right] \tag{3. 7}$$

This is the case when the only injected carriers are electrons, this is very common in most cases of APDs. If the only injected carriers are holes, the expression of excess noise factor are a little different:

$$F = M\left[1 + \left(\frac{1-k}{k}\right)\left(\frac{M-1}{M}\right)^2\right] \quad (3.\ 8)$$

In MWIR and LWIR, electrons ionization impact is dominant, and in SWIR or lower wavelength, holes ionization impact is dominant. The ratio of ionization coefficients k vs cutoff wavelength of HgCdTe relationship can be shown in *Figure 3. 10* [45]

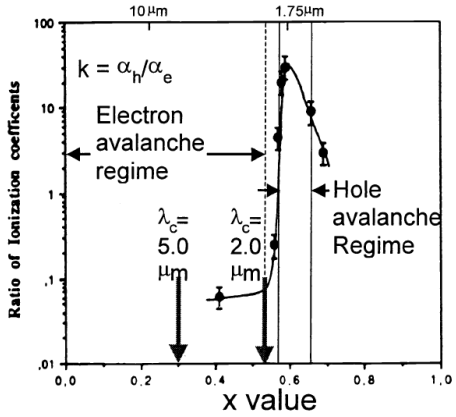

Figure 3. 8 Relation Between The Ratio of Ionization Coefficients k vs Cutoff Wavelength of HgCdTe

The local-field model theory or history-dependent model theory has been proved fit very good with GaAs APD [46][47], which is used for the wavelength from $0.1\mu m \sim 0.5\mu m$ with low gain. But in MWIR and LWIR with high gain, local-field model theory or history-dependent model cannot predict the behavior of constant excess noise factor F approximately equals to 1 in many experiment reported [39][41][42][45] as shown in *Figure 3. 11*. In high gain, the theories predict the lowest excess noise factor F should be at least 2 when $k = 0$, which contradicts the values measured in experiment.

Actually, in the condition of MWIR and LWIR with high gain, if $k = 0$, it means that holes will not appear ionization impact, which have been shown in *Figure 3. 10*. Then, the only ionization impact carriers are electrons. One electron impact other electrons to make them ionized. This
process is analogous to the stimulated photons' behavior in stimulation radiation in the laser gain medium. If we assume α to be constant, $\beta = 0$, substitute them into (3. 4), with which the multiplication gain can be reduced to an simple form:

$$M(x) = e^{\alpha x} \quad (3.\ 9)$$

This is the same expression as the laser gain expression (2. 10) with ray direction angle $\theta = 0$. So α can be explained as the gain coefficient of the APD.

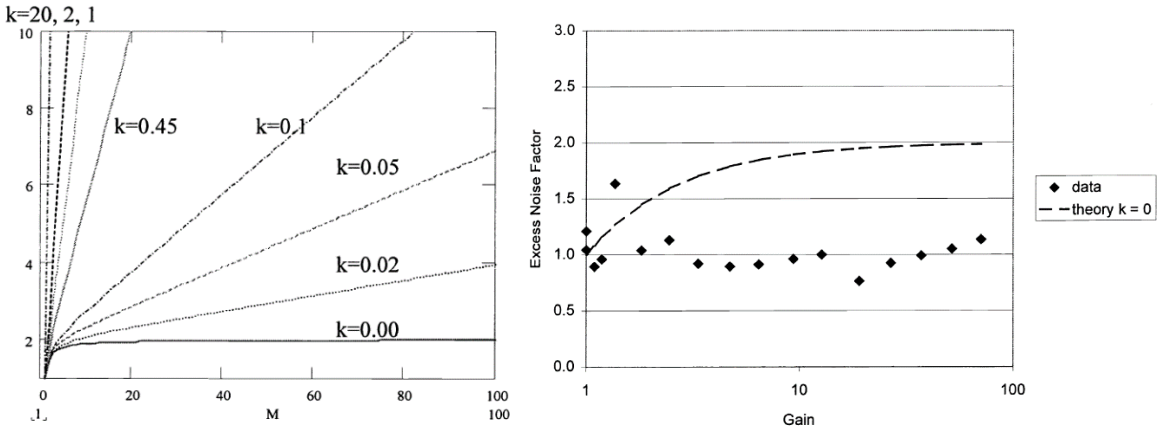

(a) (b)

Figure 3. 9 Excess Factor vs Gain: (a) Theoretical Prediction of The Excess Factor Behavior: as we can see the even the ionization coefficient factor k=0, the smallest excess factor is 2 (b) The Experimental Measurement for Excess Factor: notice that the laboratory excess factor value is measured to be constantly 1.

There are many literatures used to cite gain normalized dark current (GNDC), this is expressed as:

$$GNDC = \frac{I_{dark}}{M} \tag{3. 10}$$

Where I_{dark} is the measured dark current at the output with no input signal of APD, M is the gain of APD. In order to compare different APD detectors, gain normalized dark current density(GNDCD) is more usual to be used, this current density is normalized to the pixel size area, even though the effective optical area for the device was slightly smaller.

$$GNDCD = \frac{GNDC}{A} \tag{3. 11}$$

Where A is the area of the APD pixel, the unit of GNDCD is A/cm^2. Usually reported GNDCD ranges from $1 \times 10^{-7} A/cm^2$ to $1 \times 10^{-6} A/cm^2$ [39], which can lead to $5nA \sim 50nA$ dark current.

GNDCD is not a good sensitivity figure of merit, because in many measurement GNDCD gives an overestimation of dark current [41].There is also a more accurate sensitivity figure of merit by using the noise model of R.J. McIntyre to calculate equivalent input noise current I_{eq_in}. The relationship between shot noise of dark current i_{dark} and equivalent input noise current I_{eq_in} can be associated in this Rothman's noise model [48].

$$I_{eq\_in} = \frac{{i_{dark}}^2}{2qM^2F} = \frac{I_{dark}M_{dark}F_{dark}}{M^2F} = \frac{GNDC \cdot M_{dark}F_{dark}}{MF} \tag{3. 12}$$

Where M_{dark} and F_{dark} is the gain and excess noise factor specially for dark current . And they also give an equivalent input noise density $i_{eq\_in\_noise}(A/Hz^{\frac{1}{2}})$ definition:

$$i_{eq\_in\_noise} = \frac{i_{dark}}{M} \tag{3. 13}$$

They have given many experimental measurements but have not discussed the physical meaning of these physical variable. In this paper, we try to redefine these variables to make the noise analysis more simple. As we know shot noise spectral density is calculated with:

$$i_{shot\ noise} = \sqrt{2qI} \tag{3. 14}$$

Actually, for this reason, we can redefine equivalent input noise density $i_{eq\_in\_noise}$ as the input shot noise density $i_{shot\ noise\_in}$ of equivalent input noise current I_{eq_in}, from (3. 12) with $F = 1$:

$$i_{shot\ noise\_in} = i_{eq\_in\_noise} = \frac{i_{dark}}{M} = \frac{\sqrt{2qI_{eq\_in}M^2F}}{M} = \sqrt{2qI_{eq\_in}} \tag{3. 15}$$

With the discussion above indicated that the multiplication gain of APD should be $M(x) = e^{\alpha x}$, so there's no difference between dark current gain and signal gain $M_{dark} = M$, the error in the experiment is acceptable to recognize them as the same physical variables, and so do excess noise factor $F_{dark} = F = 1$. Then, with (3. 12) we can conclude that equivalent noise input current I_{eq_in} is the same physical variable as gain normalized dark current $GNDC$:

$$I_{eq\_in} = GNDC = \frac{I_{dark}}{M} \tag{3. 16}$$

But to be notice that the output shot noise density i_{dark} cannot be directly calculated with dark current I_{dark}:

$$i_{dark} = \sqrt{2qI_{eq\_in}M^2} = \sqrt{2qI_{dark}M} \neq \sqrt{2qI_{dark}} \tag{3. 17}$$

So the correct way to evaluate shot noise density i_{dark} of dark current is to firstly calculate shot noise density of equivalent input noise current I_{eq_in} and then multiply with the gain of APD M or directly using (3. 5) with excess factor $F = 1$. According to Rothman's measurement [48], $I_{eq\_in} = 1 \times 10^{-12}A$, GNDC= $3 \times 10^{-12}A$ at $-12.5V$ bias with gain $M = 5300$ with cutoff wavelength $\lambda_c = 5\mu m$ at $77K$. So I_{eq_in} is very closed to GNDC which proves the relation discussed above and the dark current shot noise density is $i_{dark} = 3 \times 10^{-12}A/Hz^{1/2}$, dark current is $I_{dark} = 5.3 \times 10^{-9}A$. The former is an $30\mu m$ pixel size MWIR HgCdTe APD. For LWIR HgCdTe APD, a 8×8 array $64\mu m$ pitch pixel on $9.7\mu m$ cutoff wavelength LWIR HgCdTe APD has been reported [41][42] with 1000 gain at

$10.3V$ bias, with GNDCD $1 \times 10^{-6}\ A/cm^2$(GNDC $4\times 10^{-11}A$) at $77K$. The dark current shot noise density is $i_{dark} = 3.6 \times 10^{-12}A/Hz^{1/2}$, and dark current is $I_{dark} = 4 \times 10^{-8}A$.

In our design, the signal number of photons is $\Delta N = 2.9686 \times 10^4\ s^{-1}$ with wavelength range from $3\mu m$~$10\mu m$, number of background photons is $N_{background} = 1.5265 \times 10^9 s^{-1}$. Assuming quantum efficiency is $\eta = 0.8$, so the photoelectron form an injected current:

$$I_{signal\_in} = \eta \Delta N q = 3.8 \times 10^{-15}A \quad (3.\ 18)$$

$$I_{background\_in} = \eta N_{background} q = 1.9 \times 10^{-10}A \quad (3.\ 19)$$

With $M = 1000$ gain, we have signal and background current in the output are:

$$I_{signal\_out} = MI_{signal\_in} = 3.8 \times 10^{-12}A \quad (3.\ 20)$$

$$I_{background\_out} = MI_{background\_in} = 1.9 \times 10^{-7}A \quad (3.\ 21)$$

So the signal to noise ratio can be calculated if we use LWIR HgCdTe APD as we mentioned above with bandwidth $\Delta f = 1Hz$:

$$SNR_{electricity} = \frac{{I_{singal\_out}}^2}{{i_{dark}}^2 \Delta f} = 1.11 > 1 \quad (3.\ 22)$$

If we use MWIR HgCdTe APD mentioned above with wavelength range $2\mu m$~$5\mu m$ and the gain $M = 5300$. The output currents and signal to noise ratio can be given:

$$I_{signal\_out} = 1.1 \times 10^{-12}A \quad (3.\ 23)$$

$$I_{background\_out} = 3.26 \times 10^{-8}A \quad (3.\ 24)$$

$$SNR_{electricity} = 0.13 \quad (3.\ 25)$$

Though with MWIR HgCdTe APD, $SNR_{electricity}$ is smaller than 1, we can use other methods for example lock-in amplifier to increase signal to noise ratio. These values tell us that with HgCdTe APD, infrared microscope seems possible to be realized with modern technologies.

Chapter 4. Infrared Microscope System Design

4.1 Infrared Materials Selection

The Microscope is working in the wavelength range of $3\mu m \sim 10\mu m$ to be consistent with the theoretical calculation. This wavelength range cover from MWIR ($3\mu m \sim 5\mu m$) to LWIR ($8\mu m \sim 14\mu m$). However, *Figure 4. 1* [49] shows that $5\mu m \sim 8\mu m$ is the CO_2 and water absorption band that limit our use of this spectrum within the atmosphere. The consequence is that by losing this continuum of the black body effective radiated spectrum, the SNR should decrease vastly. This is not what we expected since vital mission is to keep the SNR as large as possible. So, there is no reason to sacrifice this spectrum and instead we can put the infrared system circumvented with nitrogen or other inertia gas considering the atmospheric pressure that may damage the infrared system.

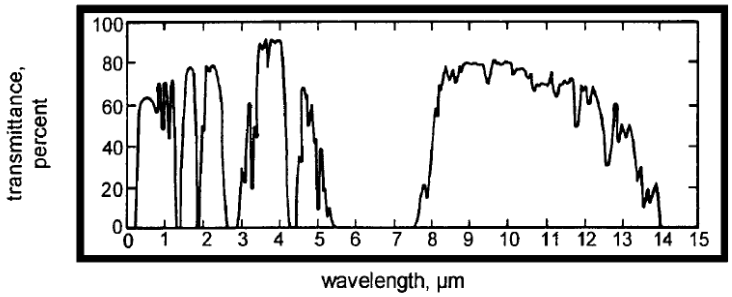

Figure 4. 1 Air Transmittance Percent in 1.8km Horizontal Air above Sea Level

There are also very limited infrared materials can be chosen as infrared lens glasses. *Figure 4. 2* [49] and *Table 4. 1* shows the traditional glasses materials transmittance and refractive index. One thing should be noted that most of applicable infrared materials have very low transmittance. Since the infrared materials also have higher refractive index compared to optical materials, they have higher reflection loss. *Figure 4. 2* is from the data including surface reflection loss, and often significantly higher transmittance results after applying high-efficiency antireflection coatings.

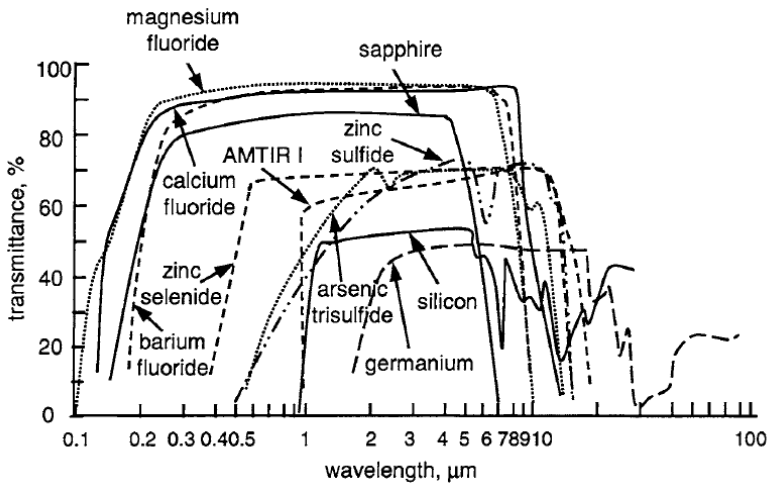

Figure 4. 2 Infrared Materials Transmittance

Material	Refractive Index		CTE (ppm/K)	dn/dT (ppm/K)	Knoop Hardness (g/mm2)	Spectral Range
	@4mm	@10mm				
Germanium	4.0243	4.0032	6	396	800	2.0 – 17.0 mm
Silicon	3.4255	N/A	2.7	150	1150	1.2 – 9.0 mm
ZnS (Cleartran)	2.2523	2.2008	4.6	54	230	0.37 – 14.0 mm
ZnSe	2.4331	2.4065	7.1	60	105	0.55 – 20.0 mm
Magnesium Fluoride	1.3526	N/A	8	20	415	0.11 – 7.5 mm
Sapphire	1.6753	N/A	5.6	13.7	1370	0.17 – 5.5 mm
Gallium Arsenide	3.3069	3.2778	5.7	148	721	0.9 – 16.0 mm
CaF_2	1.4097	1.3002	18.9	-11	170	0.13 – 10.0 mm
BaF_2	1.458	1.4014	18.4	-15	82	0.15 – 12.5 mm

Table 4. 1 Typical Infrared Glass Materials Properties

Fluoride materials such as magnesium fluoride, calcium fluoride, barium fluoride have very wide transmitted spectrum covered from UV through MWIR. This cause a problem because

we want to decrease background radiation to increase SNR for the optical signal might significantly disturb the infrared signal detection and decrease the field contrast. And most of them have undesirable hygroscopic properties that make them hard to manufacture and need to be protected from moisture damage by appropriate coating.

From *Table 4. 1* , we need to consider the transmitted spectrum and the refractive index of the applicable materials. We know infrared imaging have higher airy disc radius since the wavelength in $r = 1.22\frac{\lambda}{2NA}$ is typically higher than visible wavelength. So, the resolution in infrared system cannot be achieved as high as optical system. But at the same time, we know the typical muscular cell is about $40\mu m \sim 60\mu m$. And signal peak wavelength is about $10\mu m$. So, the resolution is really lo w compared to the cell if with typical numerical aperture $NA = 1$ and if we want to detect cell's internal metabolism. Fortunately, most of infrared materials has high refractive index that can be used to create high numerical aperture. In *Table 4. 1* , we can conclude that Germanium and GaAs are applicable materials and the transmittance can be increased with high-efficiency antireflection coatings. In our design, we choose Germanium as immersion lens material since it can increase NA to the highest degree, so we can have the best resolution.

Another option is that SCHOTT offer special infrared glasses called IRG family of Chalcogenide glasses (*Figure 4. 3*) . This glasses family has excellent transmittance as shown in *Figure 4. 4* . Most of them cover SWIR, MWIR & LWIR spectrum in a wavelength range of $0.7\mu m \sim 12\mu m$ with above 95% transmittance, which provide high flexibility in infrared system design without concerning about the signal loss. And also, they have excellent physical properties such as low dn/dT and low dispersion enable us to design color corrected optical system without thermal defocusing. And they can be single point diamond turning so that we can turn them into aspheric lens to correct high order aberration in infrared system. Typical refractive index of these glasses ranges from 2.4 to 2.9. We will not use them in the immersion lens to increase NA, but we can fully apply them in the subsequent infrared lens group in order to achieve as high transmittance as possible after combining Germanium immersion lens.

Figure 4. 3 SCHOTT IR Chalcogenide Glasses (IRG family)

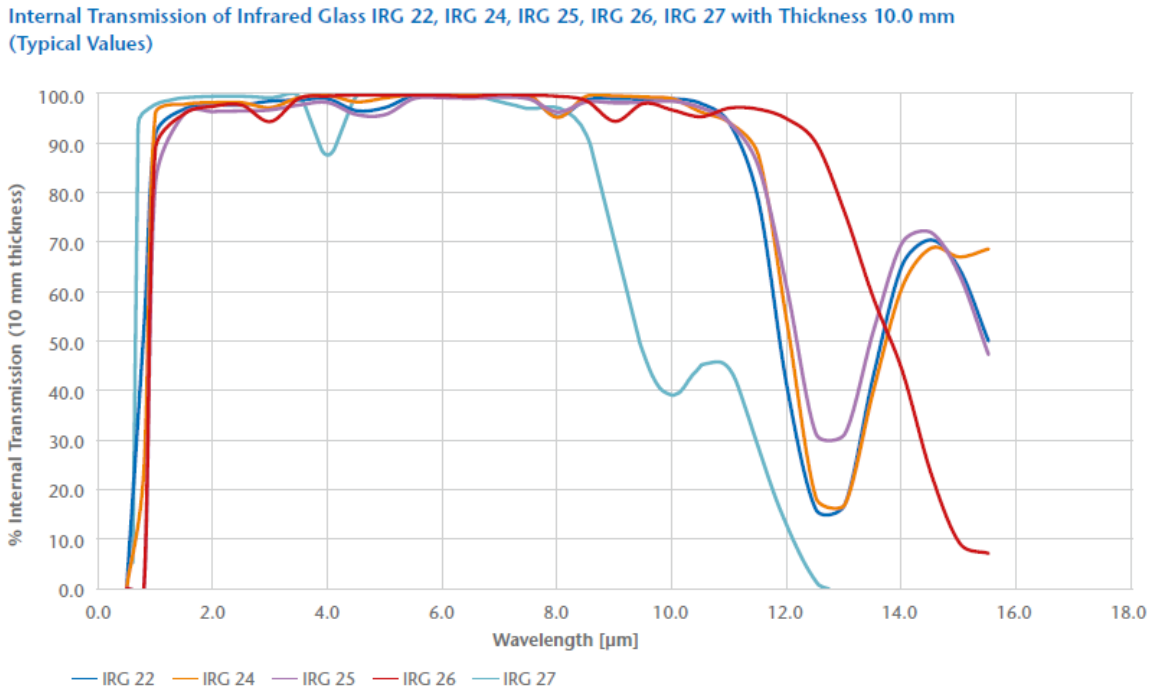

Figure 4. 4 Transmittance of IRG Glasses

4.2 Specification Determination

Traditional microscope is constituted with a magnifying objective lens that can create intermediate image. Recent modern commercial microscope is designed with infinity corrected objectives resulting in collimated beam in image space and combine a Tube lens to produce an intermediate image. The general mechanical layout can be seen in *Figure 4. 5* [50]. With this scheme, we can add scanning system and laser amplifier between objectives and tube lens to modulate optical ray beams since they are collimated.

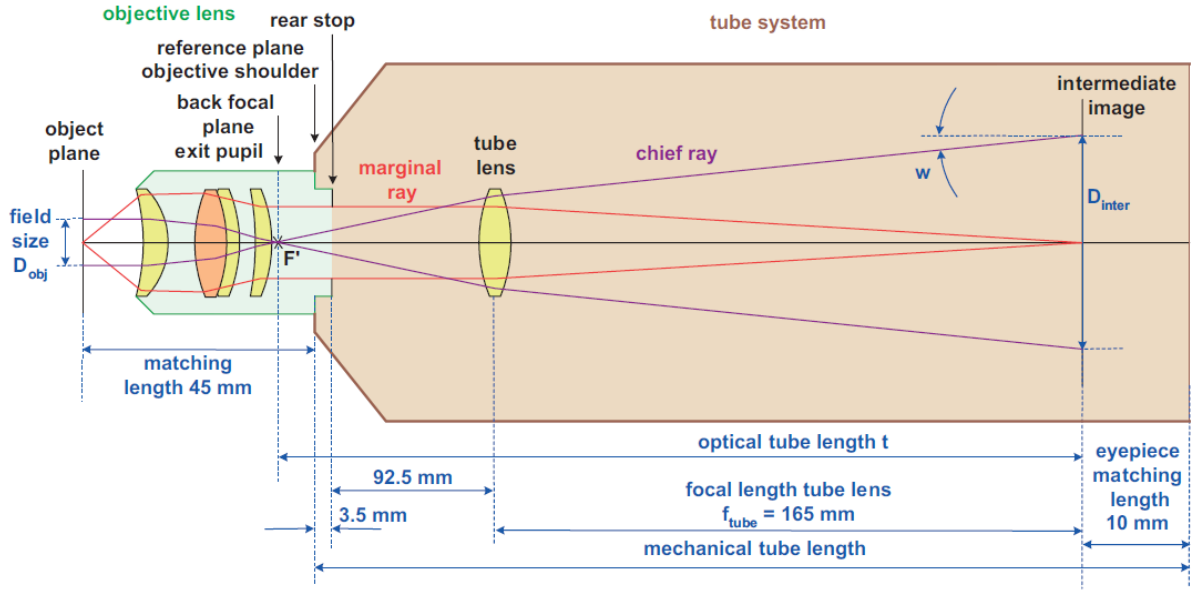

Figure 4. 5 A Sample of Objective Lens and Tube Setup For A Compound Microscope

In our design, we attempt to make this infrared system specification compatible or consistent with modern commercial optical microscope's designing standard. Standard magnification value m_{obj} of microscope objective lenses are standardized with a factor of $\sqrt[10]{10}$ between two succeeding values. This delivers the standard series of $m_{obj} = 10/12.5/16/20/25/32/40/50/63/80/100$. Manufacturers always define the size of intermediate image to a fixed diameter. The typical sizes or field numbers are $20mm, 23mm, 25mm$ or $28mm$, respectively [50]. So, we choose 60X magnification for our design. And if image field is $25mm$, with $D_{obj} = \frac{D_{img}}{m_{obj}}$, we can calculate object field of view is about $D_{obj} = 420\mu m$. In *Figure 4. 5*, most of commercial microscope's tube length (distance from exit pupil to intermediate image) are within range from $160mm \sim 200mm$ [50]76, which also indicate approximate range of the focal length of tube lens that we can choose from. In our case, we choose $f_{tube} = 180mm$. So, with equation $m_{obj} = \frac{f_{tube}}{f_{obj}}$, objective focal length should be $f_{obj} = 3mm$.

With germanium immersion lens, theoretical numerical aperture can reach to $NA = 4$. So the airy disc diameter in $10\mu m$ wavelength is $D_{airy\_10\mu m} = 2.44\frac{\lambda}{2NA} = 3\mu m$, airy disc diameter in $3\mu m$ wavelength is $D_{airy\_3\mu m} = 1\mu m$. So, the diffraction limit resolution can have a detectable diameter ranged from $1\mu m \sim 3\mu m$, which is acceptable compared to cell size, i.e. $40\mu m \sim 60\mu m$. Remember that LWIR HgCdTe APD detector's pixel pitch in chapter 3 is

64μm [42]. So, we assume we have such a detector, whose pixel pitch is $P_{img} = 60\mu m$. The detected area is $P_{obj} = \frac{P_{img}}{m_{obj}} = 1\mu m$. The cutoff frequency of the system is $\xi_{cutoff} = \frac{1}{\lambda f/\#}$, the sampling frequency is $\xi = \frac{1}{P_{obj}}$. With Nyquist's theorem, sampling frequency should satisfy the relationship $\xi \geq 2\xi_{cutoff}$. Here we introduce camera design parameter Q definition by taking the ratio of the detector sampling frequency to diffraction cutoff frequency, which is $Q = \frac{\xi}{\xi_{cutoff}} = \frac{\lambda f/\#}{P_{obj}}$. If $Q \geq 2$, the imaging system satisfy Nyquist's sampling without aliasing. But sometimes we can loose this parameter in order to get a applicable imaging system setup without strictly satisfying Nyquist's theorem. The effect of Q parameter can be shown in *Figure 4. 6*.

Figure 4. 6 Effect of Different Q Parameter in Digital Imaging System Design

If camera design parameter Q is around 2, it means optical performance balance well with detector sampling and the image will perform similar effect like the middle image shown in *Figure 4. 6* . If Q is much larger than 2, that means the optics diffraction point spread function limit the resolution, and the image tend to appear blurry just like the image on the left shown in *Figure 4. 6* . This is called optics limited. If Q is much smaller than 2, it means that sampling points are not enough, and aliasing artifacts are introduced resulting in similar effect as shown in the image on the right in *Figure 4. 6* . This is called detector limited. In our design, $Q_{10\mu m} = \frac{\xi}{\xi_{cutoff}} = \frac{\lambda}{2P_{obj}NA} = 1.25$, $Q_{3\mu m} = 0.375$. So, the system is detector limited and the sampling points are not fully enough. We need to use a detector with less pixel pitch, for example, the 30μm pixel size MWIR HgCdTe APD in Chapter 3 [41]75, the camera design parameter is $Q_{10\mu m} = 2.5$, $Q_{3\mu m} = 0.75$, which is much more properly balanced. But this detector has a cutoff wavelength in MWIR, so it is not suitable in our system design. The principle shown here is clear that we need to balance detector and optics system altogether to achieve perfect imaging matching. But since detector selection is not the most vital problem

that affects our infrared system performance, so we will stop discussing more about the improvement here.

In the end of this part, the specific attempted specifications of infrared system are listed below:

Magnification: $\mathrm{m}_{obj} = 60$
Tube lens focal length: $f_{tube} = 180mm$
Objective focal length: $f_{obj} = 3mm$
Field of View in Object height: $FOV = \pm 210mm$
Numerical aperture: $NA = 4$
Transmitted Spectrum: $\lambda = 2\mu m \sim 12\mu m$
Detector pixel pitch: $p = 60\mu m$
Detector type: LWIR HgCdTe APD
Lens Materials: Germanium, SCHOTT IRG family

4.3 Objective Design

4.3.1 Immersion Lens

Immersion Lens can be used both in image space and object space. There are two types of immersion lens, hemispherical immersion lens and hyperhemispherical immersion lens. And the magnifications of each type are $1/\mathrm{n}$, $1/\mathrm{n}^2$, respectively when used in image space and n, n^2 respectively in object space [51]. If we put the immersion lens in image space, the image is zoomed out for the magnification is below 1. That is significant in increasing signal to noise ratio for the detector's dimension is getting smaller so that the noise is decreasing as the area of detector in detectivity equation $NEP = \frac{\sqrt{A\Delta f}}{D^*}$ decreasing. If we put the immersion lens in object space, it can collect as much light as possible to increase numerical aperture and signal to noise ratio, which is very widely used in microscope optical design. Immersion lens work as aplanatic lens, so it will introduce very limited spherical, coma, astigmatism aberration. In Seidel coefficient, aplanatic condition meets with $\mathrm{A} = 0$ or $\Delta\left(\frac{\mathrm{u}}{\mathrm{n}}\right) = 0$ for hemispherical lens and hyperhemispherical lens respectively [52]. So, the object is located in concentric place in hemispherical immersion lens or with the length $\mathrm{L} = \frac{\mathrm{N}+1}{\mathrm{N}}\mathrm{R}$ from the vertex of the hyperhemispherical lens as shown in *Figure 4. 7* [51].

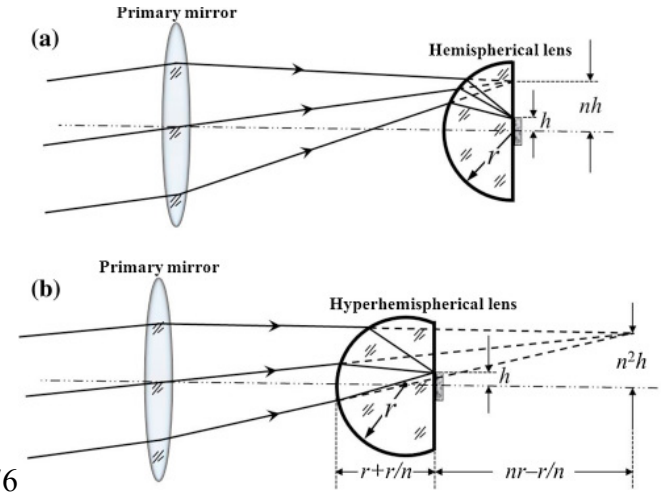

76

Figure 4. 7 Hemispherical Immersion Lens (a) and Hyperhemispherical Immersion Lens (b)

Another thing should be mentioned is that hyperhemispherical lens can increase more NA than hemispherical. If we require full NA in hemispherical lens, the aperture of the system should be very large to collect all the radiance of object that shed light in the hemisphere space. But hemispherical lens can collect all the light radiated by the object into the hemisphere with limited aperture, see *Figure 4. 8* . With aplanatic condition, we can have $\mathrm{N}\sin u' = \sin u$. So, when the object angle is $\sin u = 1$, the object ray is as steep as almost vertical to the optical axis, the image angle of the immersion lens $\sin u'$ can have limited value. The limited aperture of the system can be calculated as [51]

$$\sin u'_{\max} = \frac{1}{\mathrm{N}} = \frac{1}{\sqrt{4(\mathrm{f}/\#)^2+1}} \tag{4. 1}$$

or

$$(\mathrm{f}/\#)_{\min} = \frac{1}{2}\sqrt{\mathrm{N}^2 - 1} \tag{4. 2}$$

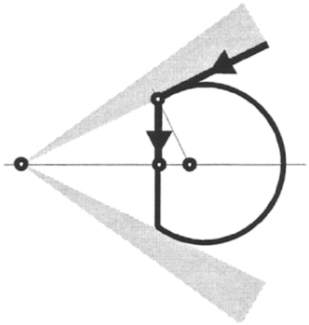

Figure 4. 8 Full NA Condition in Hyperhemispherical Lens

So that means, ideally, we can have finite aperture to collect all the light shedding from the object in the space with hyperhemispherical lens. This can increase our NA as much as possible to meet the NA potential limitation, which in our case of Germanium is approximately $\mathrm{NA} = \mathrm{N} = 4$. But another factor that affect the high numerical aperture realization is the air gap or liquid gap between the object and the flat plane of the hyperhemispherical lens. Since the evanescent wave has a decay length, if the coupling air gap or liquid gap is too large compared to the decay length, the evanescent wave cannot couple into the hyperhemispherical lens then total reflection happens on the plane surface of the immersion lens that vastly decrease the NA and the limitation of the numerical aperture, if with air gap, cannot even exceed 1. The electromagnetic wave evaluated as the composition of propagating homogeneous wave and evanescent inhomogeneous wave that couples to the immersion lens has been fully discussed in [53]. The relationship between the evanescent wave and the numerical aperture can be shown in *Figure 4. 9*. As we can see when the numerical aperture exceeds 1, the evanescent part of the electromagnetic wave contributes more energy than propagating part. One of an approach to improve this effect is by using a $1\sim3\mathrm{nm}$ roughness smoothly polished plane parallel plate substrate with one side attached to the object cell and the other attached to the immersion lens with same material [54]. The substrate and the immersion lens as a whole form a hyperhemispherical lens and the gap between the substrate and the immersion lens is short enough within the decay length to collect most of the evanescent wave. This technique is very similar to the case shown in *Figure 4. 10*.

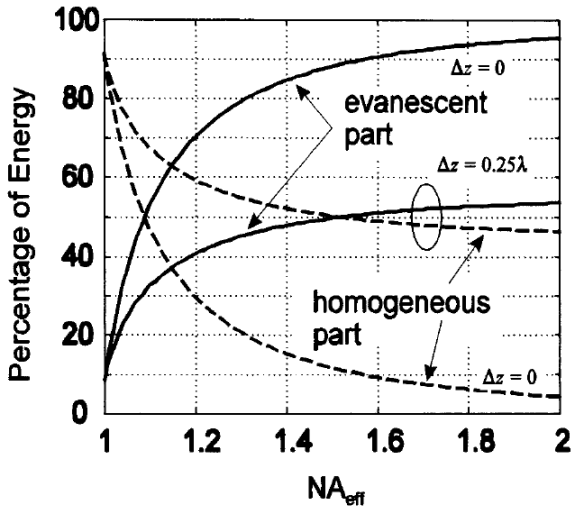

Figure 4. 9 Percentage of Energy Between Evanescent Part and Propagating Homogeneous Part

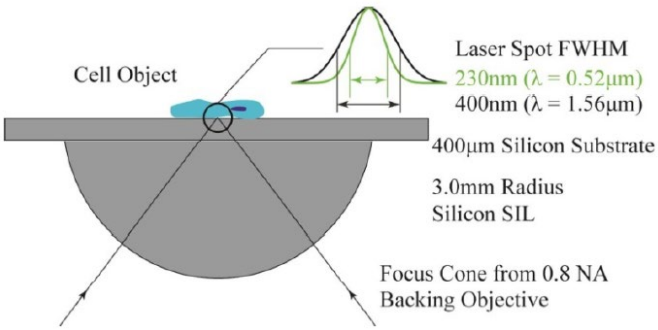

Figure 4. 10 Silicon Substrate Immersion Lens: Sample geometry using silicon sample substrate and object-centric silicon solid-immersion lens[54]

In our design, we choose hyperhemispherical lens to achieve the highest NA, and we set the immersion lens radius to be 3mm. The length of the immersion length should be $L = \frac{N+1}{N}R = 3.5mm$. But actually, in our design, Germanium has very serious total internal reflection for its high refractive index compared to the air. So, we use cemented front lens for our design. The purpose of cemented front lens is to collect the marginal rays smoothly to reduce the effect of total internal reflection as shown in *Figure 4. 11* for example [50]. the first lens Germanium and the second lens IRG family glass which have refractive index n from 2.4 to 2.9. So, the actual length of the first Germanium immersion lens is approximately $L = \frac{N+n}{N}R = 5mm$. We set this value as initiated point in our design.

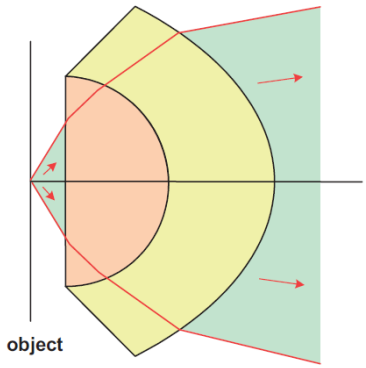

Figure 4. 11 Cemented Immersion Lens

4.3.2 The Lens Group Design Principle of the Objective [50]

The principle of microscope objective design is consistent with the designed principle of reverse telephoto objective. That is to make the effective focal length as short as possible. The objective consists of three lens groups, front part, middle part, rear part. *Figure 4. 12* shows the schematic of a typical objective constitution.

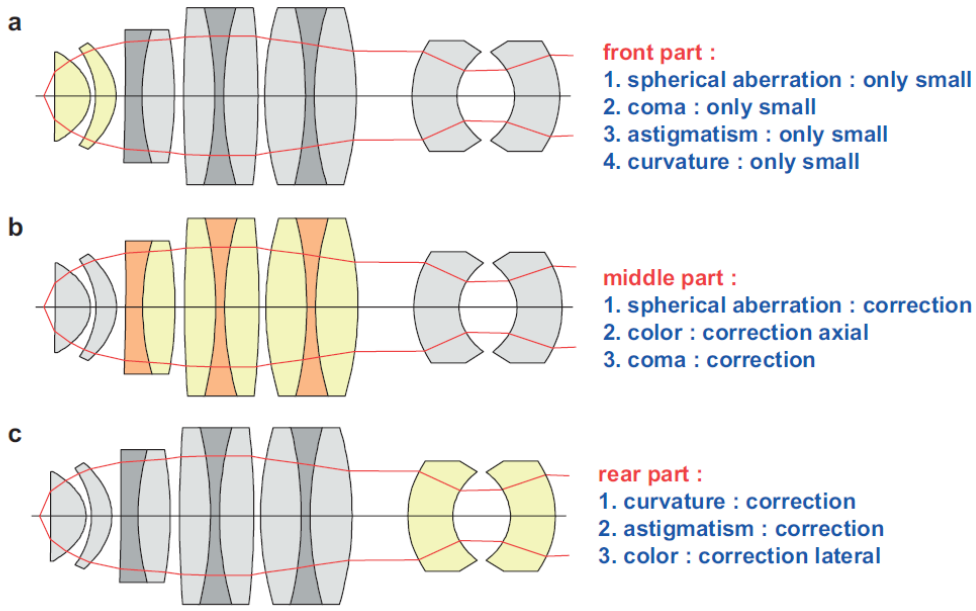

Figure 4. 12 Typical Microscope Objective Lens Group Layout

For high numerical aperture microscope objective setup, the front part is usually built with aplanatic-concentric meniscus lens and immersion lens. This shell structure ensures that in the region where bending occurs, due to large angles, no great contributions to the spherical and coma aberration will be made. The middle group is used to correct the under-correction spherical & coma aberration and color aberration contributions of the front group. So usually, they are composed of two cemented doublet or triplet for chromatic aberration or secondary chromatic aberration. The simplest middle group is composed of two doublets, we can also introduce other schematic arrangements like Double Gauss Lens or Cooke triplet to compensate astigmatism and curvature aberration as well without the rear part. In our design, we stick to the simplest method and so we need to consider the rear part. The rear group is often used for field flattener, so they are often composed of meniscus lenses to contribute the opposite Petzval sum from the previous part of the system. Also, the rear part can be used to correct astigmatism and lateral color. So finally, except for distortion, all the third order aberrations can be theoretically corrected with this microscope objective setup.

4.3.3 A Design Sample of Infrared Microscope Objective

At this part, we provide a sample of infrared microscope objective designed with Zemax. Lens data is listed in *Table 4. 2* .

Surface Number	Surface Type	Comment	Radius	Thickness	Material	Clear Semi-Diameter
	OBJECT Standard		Infinity	Infinity		Infinity
1	Standard	Dummy Surface in Object Space	Infinity	10.000		33.973
2	Standard	Meniscus Rear Part	63.016	7.000	IRG24	32.552
3	Standard	Meniscus Rear Part	348.913	74.527	IRG25	32.753
4	Standard	Meniscus Rear Part	11.977	2.800		4.189
5	Standard	Meniscus Rear Part	-6.245	32.909	IRG25	3.917
6	Standard	Meniscus Rear Part	271.363	7.000	IRG24	16.005
7	Even Asphere	Meniscus Rear Part	-32.365	0.000		16.600
		Conic	2^{nd} Order Term	4^{th} Order Term	6^{th} Order Term	8^{th} Order Term
		-0.027	-7.627E-05	-1.321E-06	-5.901E-09	5.642E-13
8	Standard	Triplet Middle Part	798.142	5.000	IRG22	15.980
9	Standard	Triplet Middle Part	-30.785	8.000	IRG25	15.956
10	Standard	Triplet Middle Part	75.381	9.500	IRG24	15.483
11	Standard	Triplet Middle Part	365.581	37.332		15.204
12	STOP Standard	Stop	Infinity	-35.564		14.400
13	Standard	Triplet Middle Part	55.228	10.500	IRG22	15.127

14	Standard	Triplet Middle Part	-18.359	5.000	IRG25	15.023
15	Standard	Triplet Middle Part	-578.587	8.000	IRG24	13.815
16	Standard	Triplet Middle Part	242.951	0.000		13.004
17	Standard	Meniscus Front Part	32.388	4.000	IRG24	12.642
18	Standard	Meniscus Front Part	40.228	0.000		11.633
19	Standard	Meniscus Front Part	11.057	4.000	IRG24	10.008
20	Standard	Meniscus Front Part	11.311	2.000		8.410
21	Standard	Immersion Lens Front Part	9.308	1.500	IRG24	6.865
22	Standard	Immersion Lens Front Part	3.074	5.076	GERMANIUM	2.693*
	IMAGE Standard	Immersion Lens Front Part	Infinity	-	GERMANIUM	0.209

Table 4. 2 Lens Data of an Infrared Microscope Objective Sample

The Cross-Section layout is shown in *Figure 4. 13*.

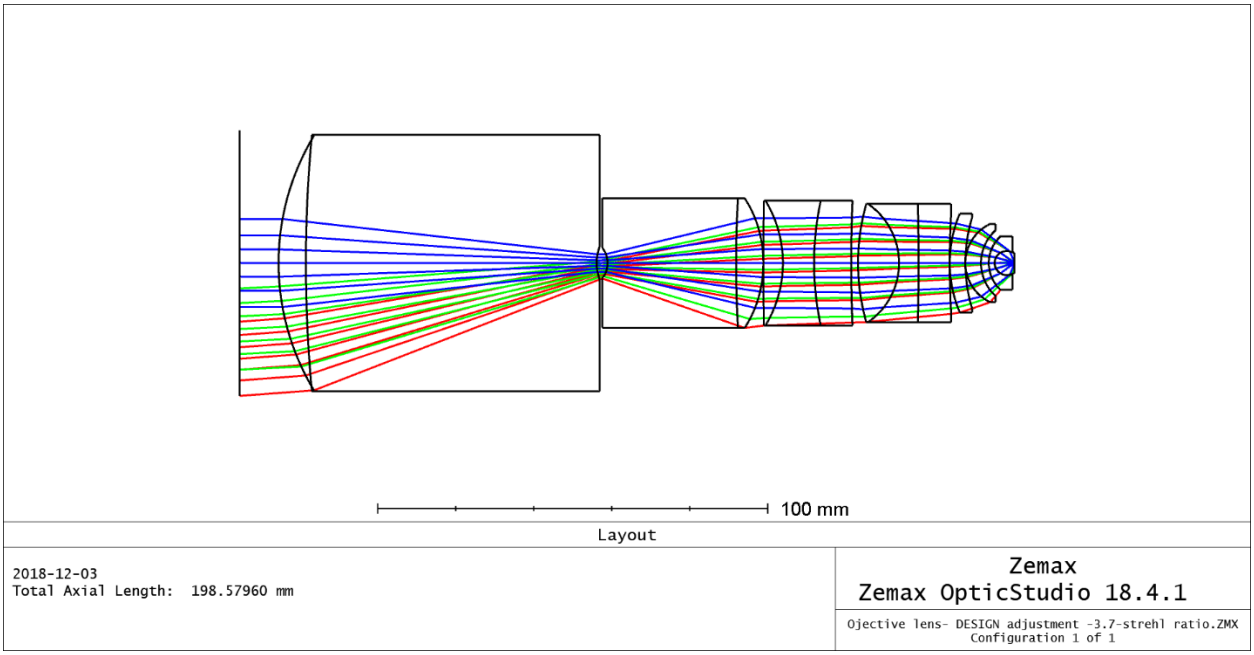

Figure 4. 13 Cross-Section Layout of a Infrared Objective Sample

The other configurations in Zemax includes:

Aperture value: 0.133 (Aperture Type: image space $F/\#$) ;
Field value: $Y = 0.000$ (Weight:1), $Y = 0.147$ (Weight:1), $Y = 0.210$ (Weight:1) ;
Wavelength: $4\mu m$ (Weight:1), $5\mu m$ (Weight:5), $7\mu m$ (Weight:10), $9\mu m$ (Weight:30), $10\mu m$
(Weight:50), $11\mu m$ (Weight:30), $12\mu m$ (Weight:1)
Ray Aiming: Real

The final achieved working $F/\#$ is $F/0.133846$, which is equivalent to $NA = 3.7$. And Field 1 ($Y = 0.000$) Strehl Ratio has been accomplished to 76.6%, Field 2($Y = 0.147$) 74.6%, Field 3($Y = 0.210$) 59.0%. The effective focal length is $f = 2.995mm$. Attempted working spectrum is $4\mu m \sim 12\mu m$, though the lens transparent spectrum may be $2\mu m \sim 12\mu m$.

The purpose of cemented immersion lens is to reduce the total internal reflection of Germanium. The following meniscus lenses are concentric-aplanatic lenses in order to bend the ray into middle lens group. The middle group composed of two triplets mainly for the correction of chromatic aberration, secondary aberration and the remaining spherical & coma

aberration. The rear group is also composed of two doublet meniscus lenses facing to each other, which can reduce field curvature, astigmatism, and lateral color aberration. We also introduce an aspheric surface in our design. But actually, this aspheric surface does not contribute too much in performance improvement. And this implies that it is not too much necessary to introduce aspheric surface. The image performance of this objective lens will be presented as followed.

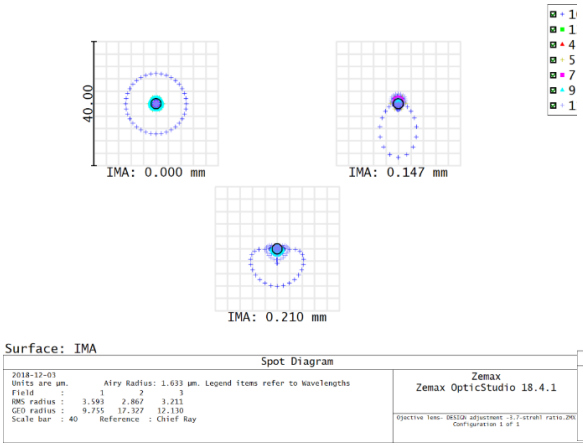

Figure 4. 14 Spot Diagram

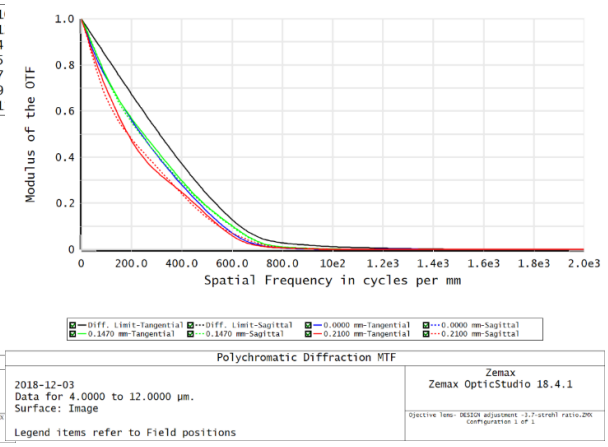

Figure 4. 15 MTF Performance

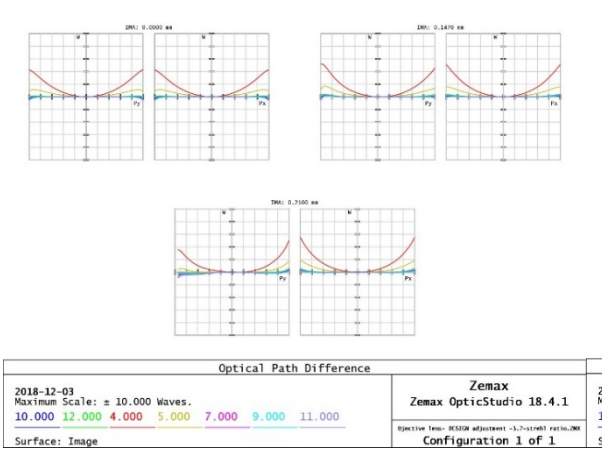

Figure 4. 16 OPD Fan

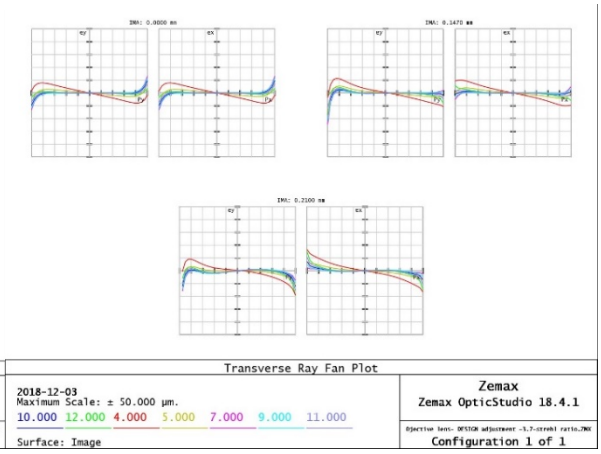

Figure 4. 17 Ray Fan

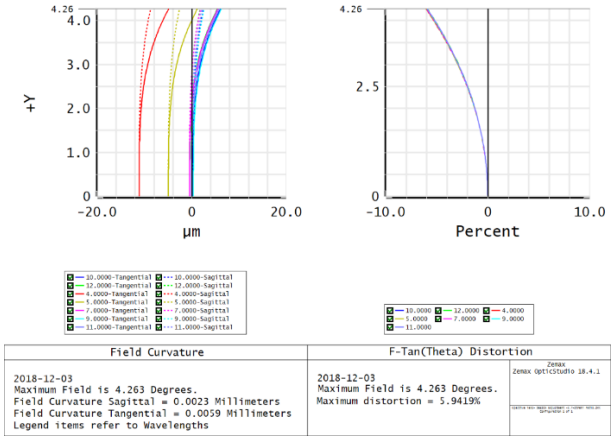

Figure 4. 18 Field Curvature and Distortion

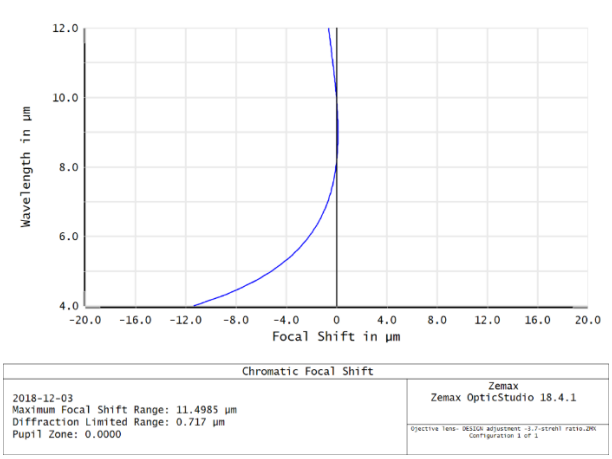

Figure 4. 19 Longitudinal Chromatic Shift

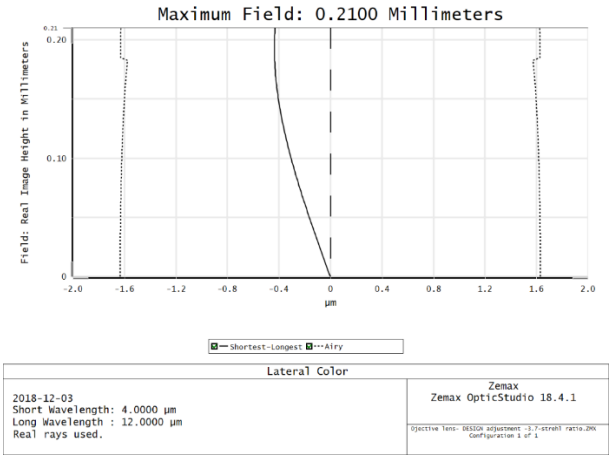

Figure 4. 20 Lateral Chromatic Shift

Figure 4. 191 Source Image in Image Simulation *Figure 4. 22 Imaging Performance in Image Simulation*

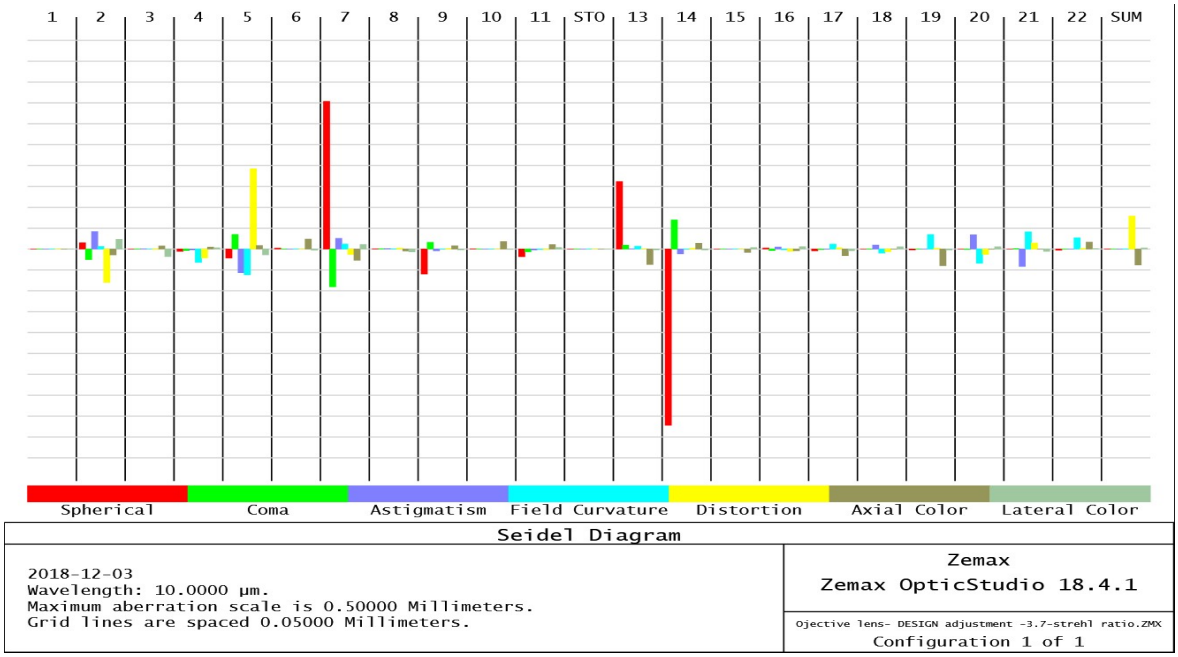

Figure 4. 20 Seidel 3rd Order Aberration Contribution in Each Surface

In this design, the most challenging aspect is the color correction. This is partially because the high dispersion in the MWIR of Germanium and IRG family glasses has not enough matched dispersion to balance the chromatic error in MWIR spectrum. This can be shown in *Figure 4. 24* . The Abbe number of Germanium in $3-5\mu m$ spectral band is really low compared to $8-12\mu m$ spectral band, which means the dispersion of Germanium in MWIR is uncommonly high. So if we try to balance MWIR and LWIR chromatic error, the secondary chromatic aberration is really high that the most useful spectrum is out of detection. So, in order to utilize the most useful spectrum, from *Figure 1. 2* , we know that we can abandon $3-5\mu m$ spectrum and make the rest $8-10\mu m$ being corrected as much as possible. That's how we did in *Figure 4. 19* , the most useful spectrum $8-10\mu m$ is lying exactly on the paraxial focus. And so, for this purpose, we should introduce a small amount of axial chromatic aberration and this can be shown in *Figure 4. 23*.

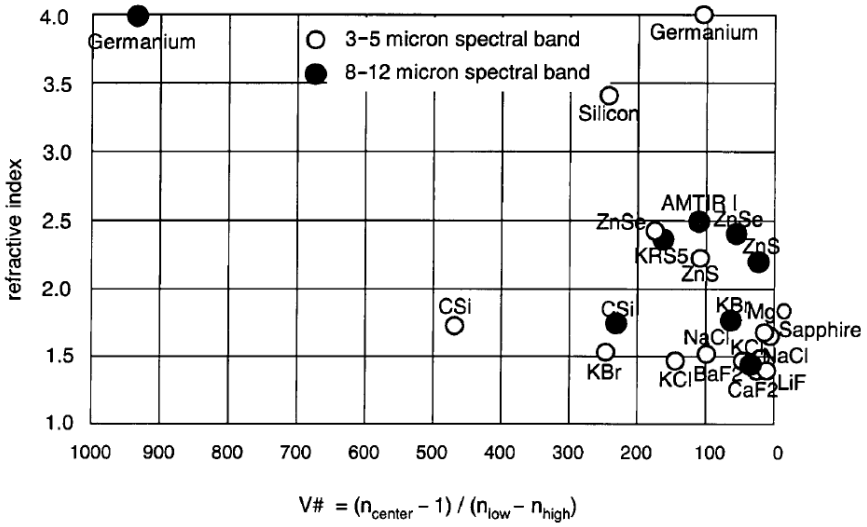

Figure 4. 21 Dispersion Relation of Infrared Materials[49]

In the future design, we can use other materials such as Silicon and GaAs in place of Germanium to achieve higher chromatic aberration correction and at the same time not to sacrifice high numerical aperture too much for their not too low refractive index compared to Germanium, if higher performance of objective is required.

4.4 Systematic Layout of Infrared microscope

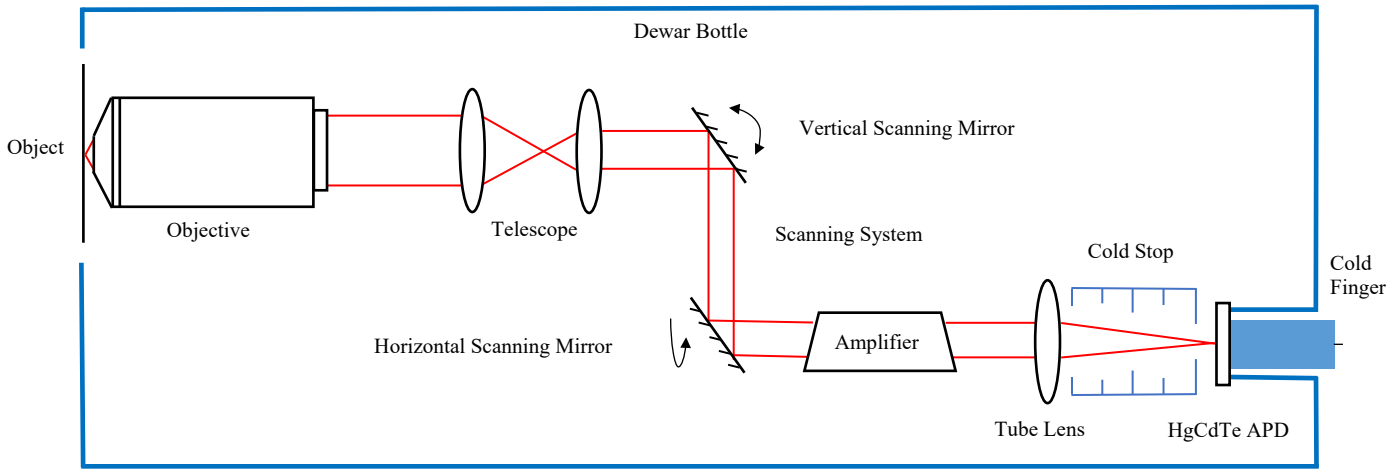

Figure 4. 22 Systematic Layout of Infrared Microscope

The infrared microscope includes basic microscopic optical system, which includes objective lens, tube lens and detector. But since the detector is a one-dimensional or small array detector, so we need two-dimensional scanning system aiding in forming full field of view

two-dimensional image. The scanning system includes telescope and two scanning mirrors. Plus, we introduce optical amplifier, for example, quantum cascade laser amplifier which has been discussed in chapter 2. In infrared system, we need to cool down the system and isolated the system with atmospheric air. The cooling system includes Dewar Bottle, cold stop, and cold finger. Specific detail in scanning system and cooling system will be evaluated as followed.

4.4.1 Scanning system [49]

Typical imaging sensor are CCD or CMOS in optical imaging system. In infrared system, a full two-dimensional detector array or focal plane array (FPA) is used similar to CCD or CMOS. But since these detectors are so costly and difficult to manufacture. For this reason, detector arrays which are smaller in extent than a full two-dimensional array are often used with appropriate scanning to allow imaging coverage over full desired two-dimensional field of view. There are two forms of scanning, one is serial scanning, the other is parallel or pushbroom scanning. Serial scanning requires two scanning mechanics one for horizontal scan and the other for vertical scan. Pushbroom scanning use a long detector array covering the entire vertical field of view so we only require horizontal scanning motion. The different mechanics can be shown simply in *Figure 4. 26* .

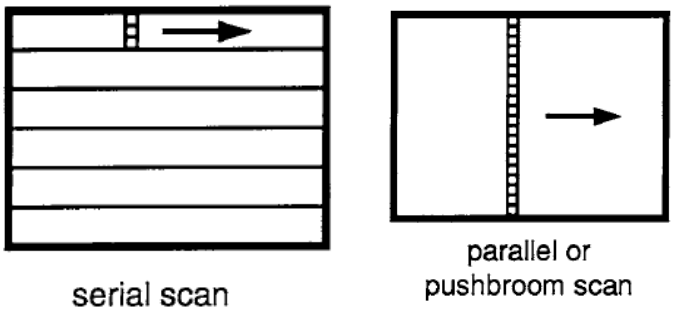

Figure 4. 23 Different Mechanics of Serial Scan and Pushbroom Scan

In *Figure 4. 25* , we can find that there's a telescope in front of the vertical scanning mirror. The purpose of the telescope is to squeeze the beam from the objective into the mirror to make the mirror small. Smaller mirror is much easier to manufacture and far less costly, also it can be used in high frequency scanning process. The other reason to use telescope is to image the exit pupil of objective exactly on the scanning mirror so that scanning process will only change chief rays but not marginal rays.

Instead of using a mirror for scanning purpose, the other commonly used scanning element is polygon mirror shown in *Figure 4. 27* . This is a rotating mirror and has a reflective surface in

each facet of the polygon. So, the polygon can continue rotating about the center and does not need to retreat to the initial point just like the flat mirror. But it happens to appear a ghost image when the polygon is rotated to the dark shaded position in *Figure 4. 27* , we can see that the ray is collected from the exterior object space or from interior structure of the system, which is called external ghosting or internal ghosting respectively. In order to prevent it, the electronics should shut off prior to the adjacent facet enters into the imaging beam of radiation. The fraction of the time that polygon is actually being used for imaging relative to the total amount of time it is running is called the scan efficiency. Scan efficiencies in the vicinity of 80% is very common.

In our system, polygon scanning mirror can be used to replace vertical scanning mirror. But in serial scan process that may require the polygon to rotate really slowly. So, to enlarge the advantage of Polygon scanning mirror, we can scan the vertical field of view much faster than horizontal scanning to make all rows fully be scanned prior to the horizontal mirror moved to the next line. The other thing to be noticed is that the rotating axis of the horizontal scanning mirror should be parallel to the exiting marginal ray direction as shown in *Figure 4. 25* . If we rotate the mirror with the axis parallel to the mirror surface, it will scan an arc not a straight line during horizontal scanning.

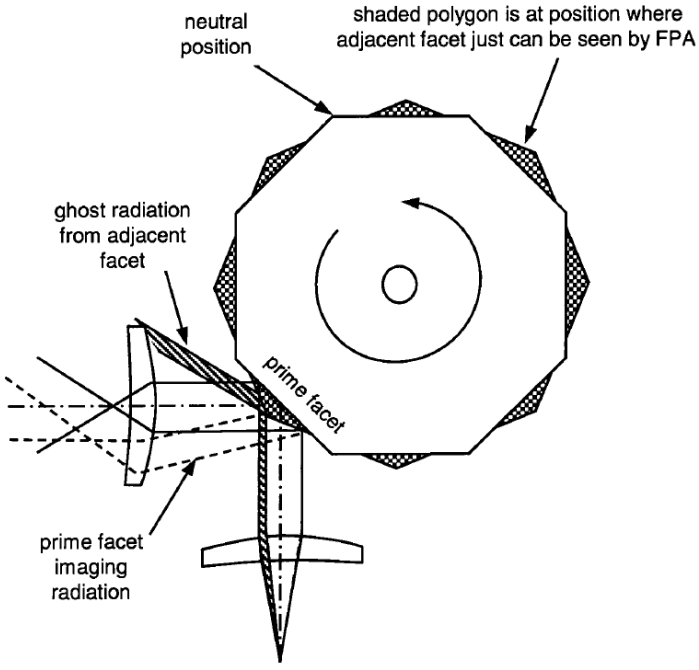

Figure 4. 24 Polygon Scanning mirror

4.4.2 Cooling System [49]

Figure 4. 25 Shows the whole infrared system is insulated by the Dewar bottle from the atmosphere. Most of thermal systems need cooling system and so does our infrared microscope especially requiring highly sensitive detection. Also, most thermal imaging systems use cryogenically cooled detectors which operate at the liquid nitrogen of 77K or even lower. Two types of HgCdTe APD discussed in this paper in chapter 3 both need to work on 77K. So, cooling system and thermal insulation system are important aspect to consider in our infrared system design.

Typical thermal insulation system is called dewar. *Figure 4. 28* shows typical generic detector/dewar assembly intended for IR-imaging application. The dewar bottle is generally an evacuated bottle very similar to classical Thermos bottle. And there is an entrance window transmitting infrared radiation. A cold finger touch against the detector to keep it cryogenically cold. The cold finger is usually a high-specific-heat metal rod of iron or steel, which is wrapped with a coil through which liquid nitrogen is pumped so that it can cool the detector. There's also a baffle called cold shield or cold stop in order to eliminate undesirable image anomalies due to background radiation for the nonscene field of view that we unwanted. The cold stop is cryogenically cold and finished with nonreflective coating, it emits little or no radiation so that the field in the solid angle outside our imaging cone blocked by the cold stop will be dark seen by the detector. But there's sometimes some leakage that cold stop cannot cover all the field outside our imaging cone. So cold stop efficiency is a notion introduced to define the ratio of the total solid angle reaching a given pixel which comes from the scene to the total solid angle reaching the same pixel from the entire opening in the thermal cold stop. *Figure 4. 29* shows the non-100% case in the left and 100% case in the right. As we can see that, the pixel may see the field outside the marginal ray in the left case and 100% cold stop efficient is achieved by making the cold stop cover the whole exit pupil which is shown in the right case in *Figure 4. 29* . Sometimes non-100% cold stop efficient is acceptable if it does not affect too much signal detection efficiency. All the cooling components in our design has been shown in *Figure 4. 25* , the difference from *Figure 4. 28* is that we must insulate the whole infrared imaging system from the atmosphere because of the atmospheric absorption window from $5\mu m - 8\mu m$ and make the dewar window as object substrate so that the objective can achieve high numerical aperture with direct contact to the object substrate.

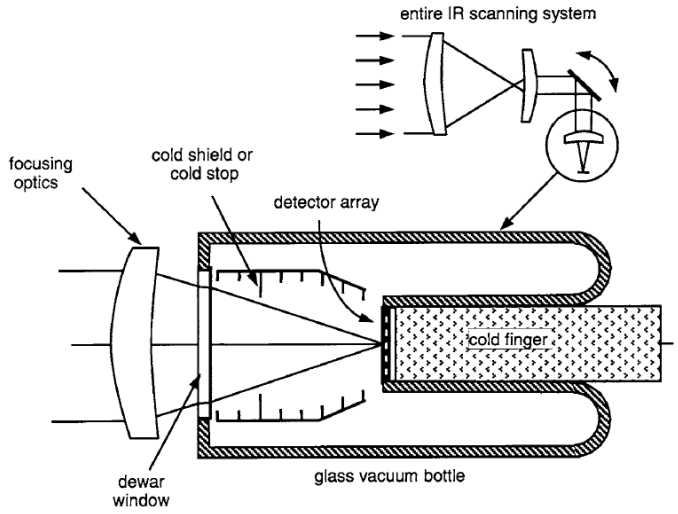

Figure 4. 25 Typical Generic Detector Dewar Assembly

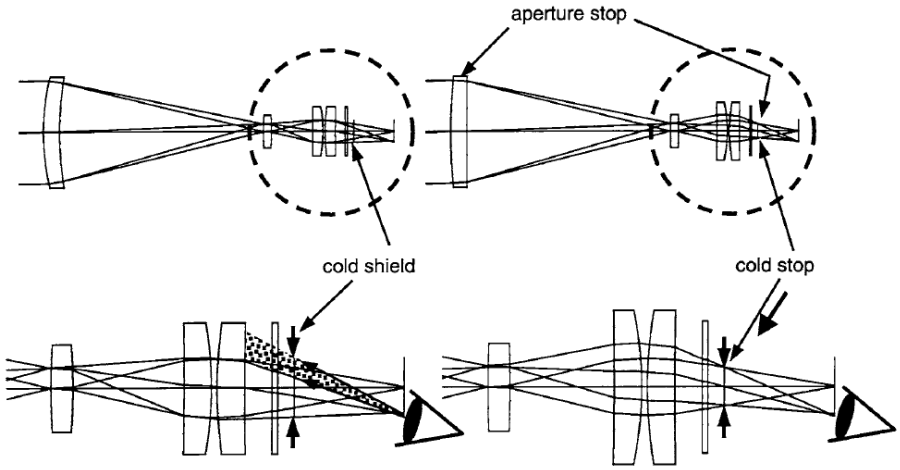

Figure 4. 26 Cold Stop Efficient: Left: System which is not 100% cold stop efficient; Right System which is 100% cold stop efficient

Chapter 5. Conclusions

So far, we have evaluated the SNR problem in the realization of infrared microscope and propose some ways to increase SNR from 10^{-8} to measurable value, for example quantum cascade laser amplifier for optical amplifier and HgCdTe PD/APD for sensitive detector. The resolution determined by the NA of objective has also been solved by designing a high NA=3.7 infrared objective and also it can increase SNR as well. All these ways combined shall we believe theoretically the experimental infrared microscope can be realized.

In addition to SNR problem discussed in this paper, there is also another problem needed to be solved in the future. That is how to increase the contrast of the microscope since the background radiation is 10^5 larger than the signal. Of course, we can decrease our requirement for lower temperature resolution so that the signal can be gathered with more photons. But the contrast is still very low even though we measure the resolution of temperature with 1K, that's meaningless since the fluctuations within the cell then is hard to be detected. So, to think of way to create dark field background is important in the microscope setup.

Also, there is another type of detector we can choose in addition to all the sensitive infrared detectors mentioned before called Type II Superlattice Detector. This is a detector comparable to Quantum Dot/Well Detector and less sensitive to HgCdTe PD. But it is still a good choice when we are going to set up the infrared microscope in the future.

Another thing needs to mention is that, even though infrared microscope is theoretically feasible, it is still very expensive and costly. Also, the available commercial choices for the detector is also very limited since the requirement of the detector is still very high to most of commercial detectors. The detectors we refer in this paper are experimental detectors, so it is still challengeable to set up an optical infrared microscope in the future. But the meaning of this paper is exactly to evaluate the difficulty and possibility to set up an infrared microscope in pure optical imaging way. We still hope that, in the future, in addition to optical imaging method we can still think of the other ways that is much more feasible and much less costly, for example, make improvement to techniques like FTIR, Raman Spectroscopy, Laser reflection and apply them to detect intracellular thermal distribution.

References

[1] Hermann, Peter, et al. "Characterization of semiconductor materials using synchrotron radiation-based near-field infrared microscopy and nano-FTIR spectroscopy." *Optics express*22.15 (2014): 17948-17958.

[2] Mordechai, Shaul, et al. "FTIR microscopic comparative study on normal, premalignant, and malignant tissues of human intenstine." *Subsurface Sensing Technologies and Applications II*. Vol. 4129. International Society for Optics and Photonics, 2000.

[3] Moreau, David, et al. "Optical measurement of temperature in biological cells under infrared laser light exposure (λ= 800 nm)." *European Conference on Biomedical Optics*. Optical Society of America, 2015.

[4] Majumdar, Annu. "Scanning thermal microscopy." *Annual review of materials science* 29.1 (1999): 505-585.

[5] Claeys, W., et al. "Thermoreflectance optical test probe for the measurement of current-induced temperature changes in microelectronic components." *Quality and Reliability Engineering International* 9.4 (1993): 303-308.

[6] Goodson, Kenneth E., and Mehdi Asheghi. "Near-field optical thermometry." *Microscale Thermophysical Engineering* 1.3 (1997): 225-235.

[7] Ostermeir, Rasso, et al. "Temperature distribution in Si-MOSFETs studied by micro-Raman Spectroscopy." *IEEE Transactions on Electron Devices* 39.4 (1992): 858-863.

[8] Naito, Yasuaki, Akio Toh-e, and Hiro-O. Hamaguchi. "In vivo time-resolved Raman imaging of a spontaneous death process of a single budding yeast cell." *Journal of Raman Spectroscopy: An International Journal for Original Work in all Aspects of Raman Spectroscopy, Including Higher Order Processes, and also Brillouin and Rayleigh Scattering* 36.9 (2005): 837-839.

[9] Cheng, Ji-xin, et al. "An epi-detected coherent anti-Stokes Raman scattering (E-CARS) microscope with high spectral resolution and high sensitivity." *The Journal of Physical Chemistry B* 105.7 (2001): 1277-1280.

[10] Sakai, Makoto, et al. "Far-field infrared super-resolution microscopy using picosecond time-resolved transient fluorescence detected IR spectroscopy." *Chemical physics letters* 439.1-3 (2007): 171-176.

[11] Inoue, Keiichi, Masaaki Fujii, and Makoto Sakai. "Development of a non-scanning vibrational sum-frequency generation detected infrared super-resolution microscope and its application to biological cells." *Applied spectroscopy* 64.3 (2010): 275-281.

[12] Lee, Eun Seong, and Jae Yong Lee. "High resolution cellular imaging with nonlinear optical infrared microscopy." *Optics Express* 19.2 (2011): 1378-1384.

[13] DeBerardinis, Ralph J., et al. "Brick by brick: metabolism and tumor cell growth." *Current opinion in genetics & development*18.1 (2008): 54-61.

[14] Cairns, Rob A., Isaac S. Harris, and Tak W. Mak. "Regulation of cancer cell metabolism." *Nature Reviews Cancer* 11.2 (2011): 85.

[15] Buck, Michael D., David O'sullivan, and Erika L. Pearce. "T cell metabolism drives immunity." *Journal of Experimental Medicine* 212.9 (2015): 1345-1360.

[16] Albright, Grant C., et al. "True temperature measurements on microscopic semiconductor targets." *Thermosense XXI*. Vol. 3700. International Society for Optics and Photonics, 1999.

[17] Riedl, Max J. *Optical design fundamentals for infrared systems*. Vol. 48. SPIE press, 2001.

[18] Milonni, Peter W., and Joseph H. Eberly. "Laser Physics." (2010).

[19] Baranov, G. A., et al. "Development of excitation system for a large-area high-pressure CO2-amplifier." *Plasma Devices and Operations* 5.3 (1997): 199-213.

[20] Corkum, P. B. "High-power, subpicosecond 10-μm pulse generation." *Optics letters* 8.10 (1983): 514-516.

[21] Stark Jr, E. E., et al. "Comparison of theory and experiment for nanosecond-pulse amplification in high-gain CO2 amplifier systems." *Applied Physics Letters* 23.6 (1973): 322-324.

[22] Buczek, C. J., R. J. Freiberg, and M. L. Skolnick. "CO2 regenerative ring power amplifiers." *Journal of Applied Physics* 42.8 (1971): 3133-3137.

[23] Cheo, P. K. "Effects of CO2, He, and N2 on the Lifetimes of the 00° 1 and 10° 0 CO2 Laser Levels and on Pulsed Gain at 10.6 μ." *Journal of Applied Physics* 38.9 (1967): 3563-3568.

[24] Kogelnik, H., and A. Yariv. "Considerations of noise and schemes for its reduction in laser amplifiers." *Proceedings of the IEEE* 52.2 (1964): 165-172.

[25] Yariv, Amnon, and J. P. Gordon. "The laser." *Proceedings of the IEEE* 51.1 (1963): 4-29.

[26] Schawlow, Arthur L., and Charles H. Townes. "Infrared and optical masers." *Physical Review* 112.6 (1958): 1940.

[27] Sirtori, Carlo, et al. "Continuous wave operation of midinfrared (7.4–8.6 μm) quantum cascade lasers up to 110 K temperature." *Applied physics letters* 68.13 (1996): 1745-1747.

[28] Rosfjord, Kristine M., et al. "Nanowire single-photon detector with an integrated optical cavity and anti-reflection coating." *Optics express* 14.2 (2006): 527-534.

[29] Dorenbos, S. N., et al. "Low gap superconducting single photon detectors for infrared sensitivity." *Applied Physics Letters* 98.25 (2011): 251102.

[30] Mc Manus, M. K., et al. "PICA: Backside failure analysis of CMOS circuits using Picosecond Imaging Circuit Analysis." *Microelectronics Reliability* 40.8-10 (2000): 1353-1358.

[31] Niigaki, M., et al. "Field-assisted photoemission from InP/InGaAsP photocathode with p/n junction." *Applied physics letters* 71.17 (1997): 2493-2495.

[32] Hamamatsu PMT handbook “Photomultiplier Tubes” 3rd edition

[33] Mariella Jr, Raymond P., and Gregory A. Cooper. "Infrared-sensitive photocathode." U.S. Patent No. 5,404,026. 4 Apr. 1995.

[34] Ryzhii, V., et al. "Comparison of dark current, responsivity and detectivity in different intersubband infrared photodetectors." *Semiconductor science and technology* 19.1 (2003): 8.

[35] Levine, B. F. "Quantum-well infrared photodetectors." *Journal of applied physics* 74.8 (1993): R1-R81.

[36] Levine, B. F., et al. "Normal incidence hole intersubband absorption long wavelength GaAs/Al x Ga1− x As quantum well infrared photodetectors." *Applied physics letters* 59.15 (1991): 1864-1866.

[37] Phillips, Jamie. "Evaluation of the fundamental properties of quantum dot infrared detectors." *Journal of Applied Physics*91.7 (2002): 4590-4594.

[38] Vaillancourt, Jarrod, et al. "Low-bias, high-temperature operation of an InAs–InGaAs quantum-dot infrared photodetector with peak-detection wavelength of 11.7 μm." *Infrared Physics & Technology* 52.1 (2009): 22-24.

[39] Norton, P. "HgCdTe infrared detectors." *Optoelectronics review* 3 (2002): 159-174.

[40] McIntyre, R. J. "Multiplication noise in uniform avalanche diodes." *IEEE Transactions on Electron Devices* 13.1 (1966): 164-168.

[41] Perrais, Gwladys, et al. "Gain and dark current characteristics of planar HgCdTe avalanche photo diodes." *Journal of electronic materials* 36.8 (2007): 963-970.

[42] Beck, Jeff, et al. "The HgCdTe electron avalanche photodiode." *Journal of electronic materials* 35.6 (2006): 1166-1173.

[43] Yuan, P., et al. "A new look at impact ionization-Part II: Gain and noise in short avalanche photodiodes." *IEEE Transactions on Electron Devices* 46.8 (1999): 1632-1639.

[44] McIntyre, R. J. "A new look at impact ionization-Part I: A theory of gain, noise, breakdown probability, and frequency response." *IEEE Transactions on Electron Devices* 46.8 (1999): 1623-1631.

[45] Beck, Jeffrey D., et al. "MWIR HgCdTe avalanche photodiodes." *Materials for Infrared Detectors*. Vol. 4454. International Society for Optics and Photonics, 2001.

[46] Bulman, G. E., et al. "Experimental determination of impact ionization coefficients in." *IEEE Electron Device Letters* 4.6 (1983): 181-185.
[47] Hu, C., et al. "Noise characteristics of thin multiplication region GaAs avalanche photodiodes." *Applied physics letters* 69.24 (1996): 3734-3736.
[48] Rothman, J., et al. "High performance characteristics in pin MW HgCdTe e-APDs." *Infrared Technology and Applications XXXIII*. Vol. 6542. International Society for Optics and Photonics, 2007
[49] Fischer, Robert Edward, et al. *Optical system design*. New York: McGraw Hill, 2000.
[50] Herbert Gross, eds. *Handbook of optical systems, volume 4: Survey of Optical Instruments*. Wiley-VCH, 2008
[51] Riedl, Max J. *Optical design fundamentals for infrared systems*. Vol. 48. SPIE press, 2001.
[52] Welford, W. (1986). Aberrations of Optical Systems. New York: Routledge,
[53] Milster, Tom D., Joshua S. Jo, and Kusato Hirota. "Roles of propagating and evanescent waves in solid immersion lens systems." *Applied optics* 38.23 (1999): 5046-5057.
[54] Kim, Youngsik, et al. "Hyper-numerical aperture (NA= 2.8) microscope using λ= 1.56 μm femtosecond source for multi-photon imaging." *Biomedical optics express* 4.10 (2013): 1786-1794.
[55] Betzig, Eric, et al. "Near field scanning optical microscopy (NSOM): development and biophysical applications." *Biophysical journal* 49.1 (1986): 269-279.
[56] Okabe, Kohki, et al. "Intracellular temperature mapping with a fluorescent polymeric thermometer and fluorescence lifetime imaging microscopy." *Nature communications* 3 (2012): 705.
[57] Brites, Carlos DS, et al. "Thermometry at the nanoscale." *Nanoscale* 4.16 (2012): 4799-4829.